The Astrophysical Journal, 925:42 (27pp), 2022 January 20 https://doi.org/10.3847/1538-4357/ac3753
© 2022. The Author(s). Published by the American Astronomical Society.
OPEN ACCESS

Magnetically Induced Anisotropies in the Arrival Directions of Ultra-high-energy Cosmic Rays from Nearby Radio Galaxies

Cainã de Oliveira and Vitor de Souza
Instituto de Física de São Carlos, Universidade de São Paulo, Av. Trabalhador São-carlense 400, São Carlos, Brasil; caina.oliveira@usp.br, vitor@ifsc.usp.br
Received 2021 August 18; revised 2021 October 19; accepted 2021 November 4; published 2022 January 24

Abstract

Detailed simulations of the arrival directions of ultra-high-energy cosmic rays are performed under the assumption of strong and structured extragalactic magnetic field (EGMF) models. Particles leaving Centaurus A, Virgo A, and Fornax A are propagated to Earth, and the simulated anisotropic signal is compared to the dipole and hotspots published by the Pierre Auger and Telescope Array Collaborations. The dominance of the EGMF structure in the arrival directions of events generated in local sources is shown. The absence of events from the Virgo A direction is related to the strong deviation caused by the EGMF. Evidence that these three sources contribute to an excess of events in the direction of the three detected hotspots is presented. Under the EGMF considered here, M82 is shown to have no contribution to the hotspot measured by the Telescope Array Observatory.

Unified Astronomy Thesaurus concepts: Ultra-high-energy cosmic radiation (1733); Extragalactic radio sources (508); Extragalactic magnetic fields (507); Cosmic ray sources (328)

1. Introduction

The detection of ultra-high-energy cosmic-ray sources is one of the most important open questions in astrophysics. The identification of only one source would open a new window of discoveries concerning the balance and transfers of energy in extremely powerful objects. The lack of knowledge about the source position and type introduces several uncertainties in the interpretation of the data, representing a major barrier for the progress toward describing the most energetic phenomena in nature. Given that ultra-high-energy cosmic rays (UHECRs) are charged, the main challenges to overcome are the unknowns about the structure and intensity of the magnetic fields in the universe.

The Pierre Auger (The Pierre Auger Collaboration 2015) and the Telescope Array (The Telescope Array Collaboration 2008) Observatories have detected the more precise UHECR signals from the sky. Three regions with a relative excess of events (hotspots) in the arrival directions of UHECRs have been identified: two regions in the Pierre Auger Observatory data (The Pierre Auger Collaboration 2018a) and one region in the Telescope Array data (The Telescope Array Collaboration 2014). A small level of anisotropy was also detected in the arrival directions of events measured by the Pierre Auger Observatory, in which a dipole signal was reported (The Pierre Auger Collaboration 2017, 2018b). A correlation of the arrival directions of events with the supergalactic plane has been reported by the Telescope Array Collaboration (The Telescope Array Collaboration 2020) and an indication of a correlation with starburst regions has been reported by the Pierre Auger Observatory (The Pierre Auger Collaboration 2018a).

The relation of these signals to the sources is not straightforward because deviations caused by the magnetic fields on the way to Earth blur, relocate, or erase the direction of the source in the sky maps. The importance of the Galactic and extragalactic magnetic field intensity and structure has been explored in the past by many authors (Lee et al. 1995; Sigl et al. 2004; Tanco 2001, 1998; Jansson & Farrar 2012; Lang et al. 2020; Erdmann et al. 2016). The dipole measured by the Pierre Auger Observatory points away from the Galactic plane and center, suggesting an extragalactic origin of UHECR. The amplitude of the dipole increases with energy above 4 EeV, suggesting an increase in the relative contribution to the flux arriving at Earth from the nearby sources (The Pierre Auger Collaboration 2017, 2018b). Despite the exact coordinates of one of the hotspots measured by the Pierre Auger Observatory not being published, it seems to be related to the direction of the radio galaxy Centaurus A (The Pierre Auger Collaboration 2018a). The starburst region M82 has been proposed as the source of the hotspot measured by the Telescope Array Observatory (The Telescope Array Collaboration 2014). The lack of an excess in the data of the Pierre Auger Observatory in the direction of Virgo A has called the attention of several authors (Dolag et al. 2009; Kobzar et al. 2019).

Radio galaxies have been considered prime source candidates (Ginzburg & Syrovatskii 1963). Several models have been proposed to describe acceleration mechanisms able to generate UHECRs in radio galaxies. Most of the models correlate the UHECR flux emitted by radio galaxies with the jet power (Pacholczyk 1970; Rachen & Biermann 1993; Eichmann et al. 2018; Eichmann 2019; Matthews et al. 2019), which in turn can be related to the radio luminosity (Godfrey & Shabala 2016; Cavagnolo et al. 2010). In this scenario, the radio galaxies Centaurus A (NGC 5128), Virgo A (NGC 4486), and Fornax A (NGC 1316) should produce a significant percentage of the UHECR flux arriving at Earth because they have a radio flux about one order of magnitude above other nearby radio galaxies (Ginzburg & Syrovatskii 1963; van Velzen et al. 2012) and because of their proximity (<21 Mpc). Besides that, it has been pointed out that nearby sources are needed to explain not only the arrival direction data but also the energy spectrum and composition measurements (Taylor et al. 2011; Lang et al. 2020, 2021).

Original content from this work may be used under the terms of the Creative Commons Attribution 4.0 licence. Any further distribution of this work must maintain attribution to the author(s) and the title of the work, journal citation and DOI.

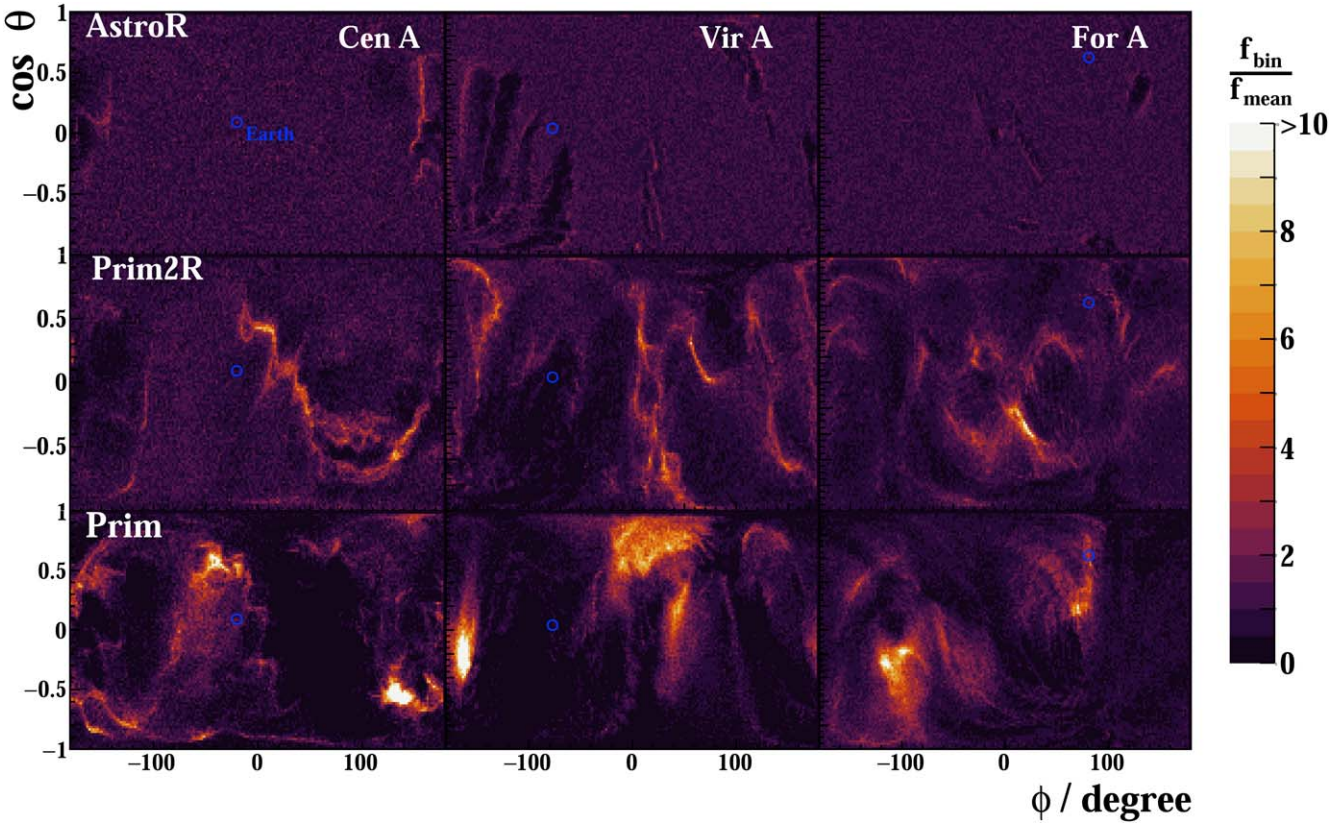

Figure 1. Relative flux of UHECRs around Cen A, Vir A, and For A. Each line in the figure shows one EGMF model: AstroR, Prim2R, and Prim. Each column in the figure shows the results for one source: Cen A, Vir A, and For A. Particles were tracked from the source (center of the map) until they reached a sphere with radius equal to the distance from the source to Earth. The maps show the arrival position of all particles in this sphere. The blue circle shows the position of Earth. The color code in the maps represents the relative flux of UHECR. All nuclei are considered to leave the source with equal flux.

In this paper, detailed simulations of arrival direction maps of particles produced in Centaurus A, Virgo A, and Fornax A are presented. The details of the simulations are given in Section 2. Special treatment of the local extragalactic magnetic field is considered. In comparison to the methodology of previous works (Lee et al. 1995; Tanco 2001, 1998; Sigl et al. 2003, 2004), this paper introduces recent models of the structure of the local extragalactic magnetic field (Hackstein et al. 2018) in full three-dimensional simulations (Batista et al. 2016). It is also shown here for the first time that the structure of the local extragalactic magnetic field is determinant to understand the signals of UHECR anisotropy detected by the Pierre Auger and Telescope Array Observatories.

The effects of the structure of the extragalactic magnetic fields are discussed in Section 3, and the deficit in the direction of Virgo A is explained. The dipole signal is explored in Section 3.1, and the possibility of explaining its direction only with events from Centaurus A, Virgo A, and Fornax A is discussed. The hotspots are discussed in Section 3.2 and possible counterparts with Centaurus A, Virgo A, and Fornax A are presented. The work is summarized in Section 4.

2. Method: The Sources, the Medium, and the Propagation

Some source types have been proposed to accelerate UHECRs (Hillas 1984; Olinto 2000; Wang et al. 2008; Dermer & Razzaque 2010; Ghisellini et al. 2008; Halzen & Hooper 2002; Rachen & Mészáros 1998; Vietri 1995; Waxman 1995; Mannheim & Biermann 1989), among which radio galaxies are one of the most accepted candidates (Rachen 2008; Romero et al. 1996; Norman et al. 1995; Bell et al. 2018; Eichmann et al. 2018; Matthews et al. 2019). Centaurus A (Cen A), Virgo A (Vir A), and Fornax A (For A) are the most powerful nearby radio galaxies. Their radio luminosities at a frequency of 1.1 GHz, $L_{1.1}$, are $L_{1.1}^{\rm CenA} = 2.6 \times 10^{40}$ erg s^{-1}, $L_{1.1}^{\rm VirA} = 7.6 \times 10^{40}$ erg s^{-1}, and $L_{1.1}^{\rm ForA} = 8.3 \times 10^{40}$ erg s^{-1} (van Velzen et al. 2012), an order of magnitude higher than that of other nearby radio galaxies. They are relatively close to Earth with distances: $D^{\rm CenA} = 3.8$ Mpc, $D^{\rm VirA} = 18.4$ Mpc, and $D^{\rm ForA} = 20.9$ Mpc. The combination of high radio power and proximity makes them strong candidates for dominating the UHECR sky. Reviews of these sources can be found in the following references: Israel (1998), Rejkuba (2004), Ferrarese et al. (2006), Macchetto et al. (1997), Röser & Meisenheimer (1997), Jensen et al. (2003), Schweizer (1980), and Nowak et al. (2008).

In this paper, UHECRs are injected from Cen A, Vir A, and For A and propagated to Earth on computational simulations. Each of the three sources has been extensively studied as possible UHECR sources (Romero et al. 1996; Kachelriess et al. 2009; Biermann et al. 2010; Biermann & De Souza 2012; Wykes et al. 2013; Matthews et al. 2018; Kobzar et al. 2019). It is not in the scope of this paper to discuss the acceleration models in the sources. Therefore, a standard first-order Fermi acceleration (Kotera & Olinto 2011) in the diffusive shock of active galactic nucleus (AGN) jets (Matthews et al. 2019) has been used. In this scenario, the UHECR injection spectrum is given by a power law with a charge-dependent exponential

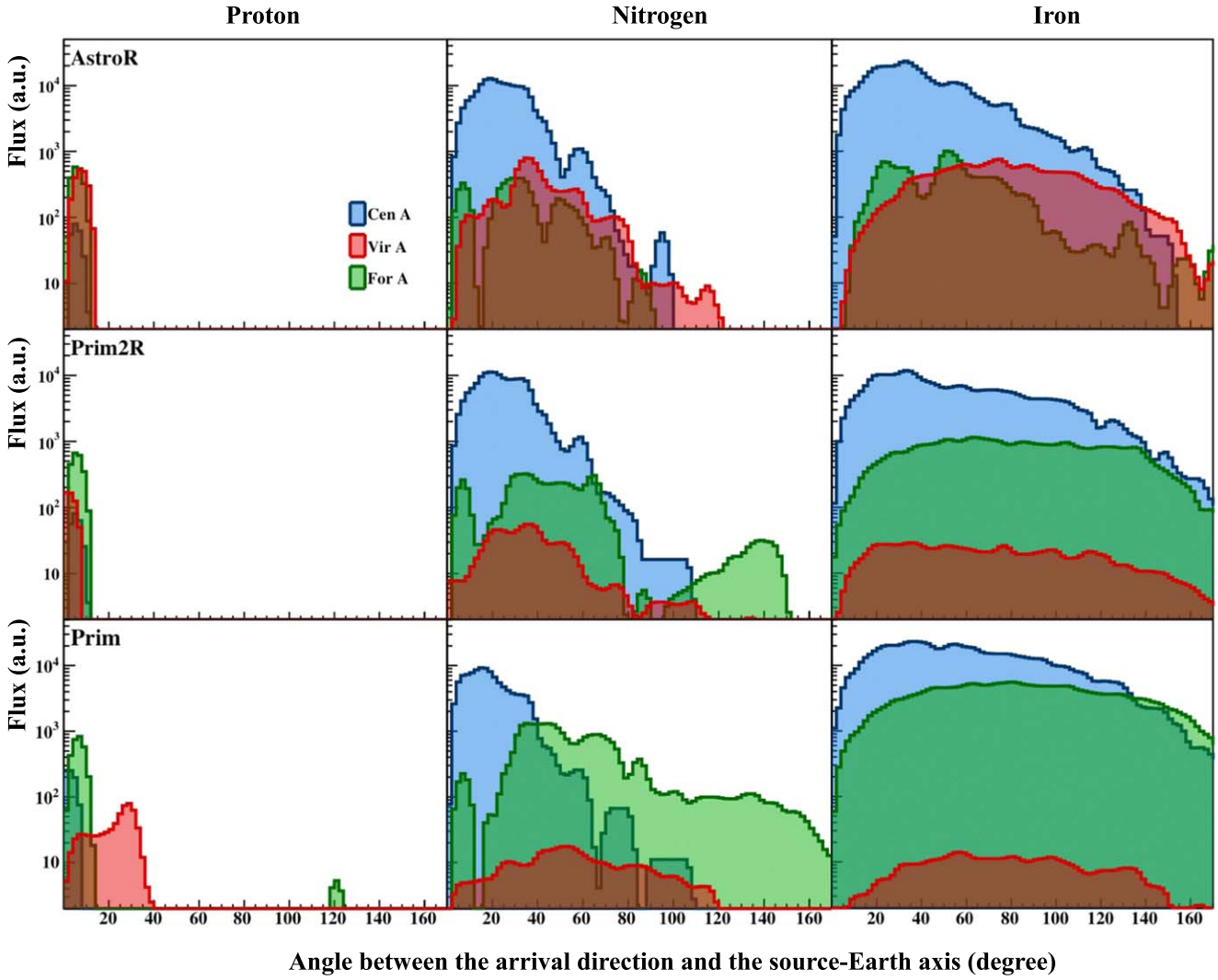

Figure 2. Angular distribution of events with $E > 32$ EeV in relation to the source direction. Each line in the figure shows one EGMF model: AstroR, Prim2R, and Prim. Each column in the figure shows a different nucleus leaving the source: proton, nitrogen, and iron nuclei. Note that in each column of the figure, all nucleus fragments on their way to Earth are shown as arriving at Earth although only proton, nitrogen, or iron nuclei left the source. The three sources are differentiated by color: blue, red, and green for Cen A, Vir A, and For A, respectively. The sources are considered to output the same UHECR flux.

cutoff (Supanitsky & de Souza 2013). Details are given in Appendix A.

UHECRs interact with radiation and magnetic fields on their way from the source to Earth, changing their properties. The CRPropa3 framework (Batista et al. 2016) was used to propagate particles from their sources to Earth. A very time-consuming 3D simulation was done with 3×10^8 events for each source for each nuclei: ^{1}H (proton), ^{2}He, ^{7}N, ^{14}Si, and ^{26}Fe, with injected energies between 10^{18} and 10^{21} eV following a power-law spectrum with spectrum index -1 to guarantee equal statistical uncertainties at all energies. The particles were emitted isotropically from the source. After propagation, the energy spectrum was weighted according to the explanation in Appendix A. The energy-loss mechanisms and interactions considered are pion photoproduction, pair production, photodisintegration, nuclear decay, and adiabatic loss. UHECRs are propagated until they reached the surface of a sphere with a radius ($r_{\rm obs}$) centered on Earth. The radius ($r_{\rm obs}$) was set to $r_{\rm obs}^{\rm CenA} = 100$ kpc, $r_{\rm obs}^{\rm VirA} = 400$ kpc, and $r_{\rm obs}^{\rm ForA} = 500$ kpc, depending on the source in consideration. The variable value of $r_{\rm obs}$ minimizes the number of simulated events, saving computational time, and guarantees an uncertainty in the arrival direction of events from each source (Hackstein et al. 2016) smaller than the uncertainties in the arrival direction measurements (The Pierre Auger Observatory 2020). A smaller set of events was also simulated for an observational radius of 10 kpc for all sources. The conclusions presented here remain the same irrespective of $r_{\rm obs}$. The artificial uncertainty due to the finite observer can be estimated as $\arcsin(r_{\rm obs}/D)$, if the magnetic field in the observer neighborhood is not too intense; therefore, if $r_{\rm obs} = 100$ kpc and $D_{\rm source} = 10$ Mpc then the artificial deflection is $0.01 < 1$, and if $r_{\rm obs} = 10$ kpc the artificial deflection becomes one order of magnitude smaller.

The background photon fields considered in this paper are the cosmic microwave background and the extragalactic background light (Gilmore et al. 2012). The photon fields have an important effect on the propagation of UHECRs even for nearby sources. The interaction of UHECRs with the gas surrounding the sources can be safely ignored given that the baryon content have a estimated density on the filaments of massive galaxy clusters of $\approx 10^{-5}$ cm^{-3} (Eckert et al. 2015);

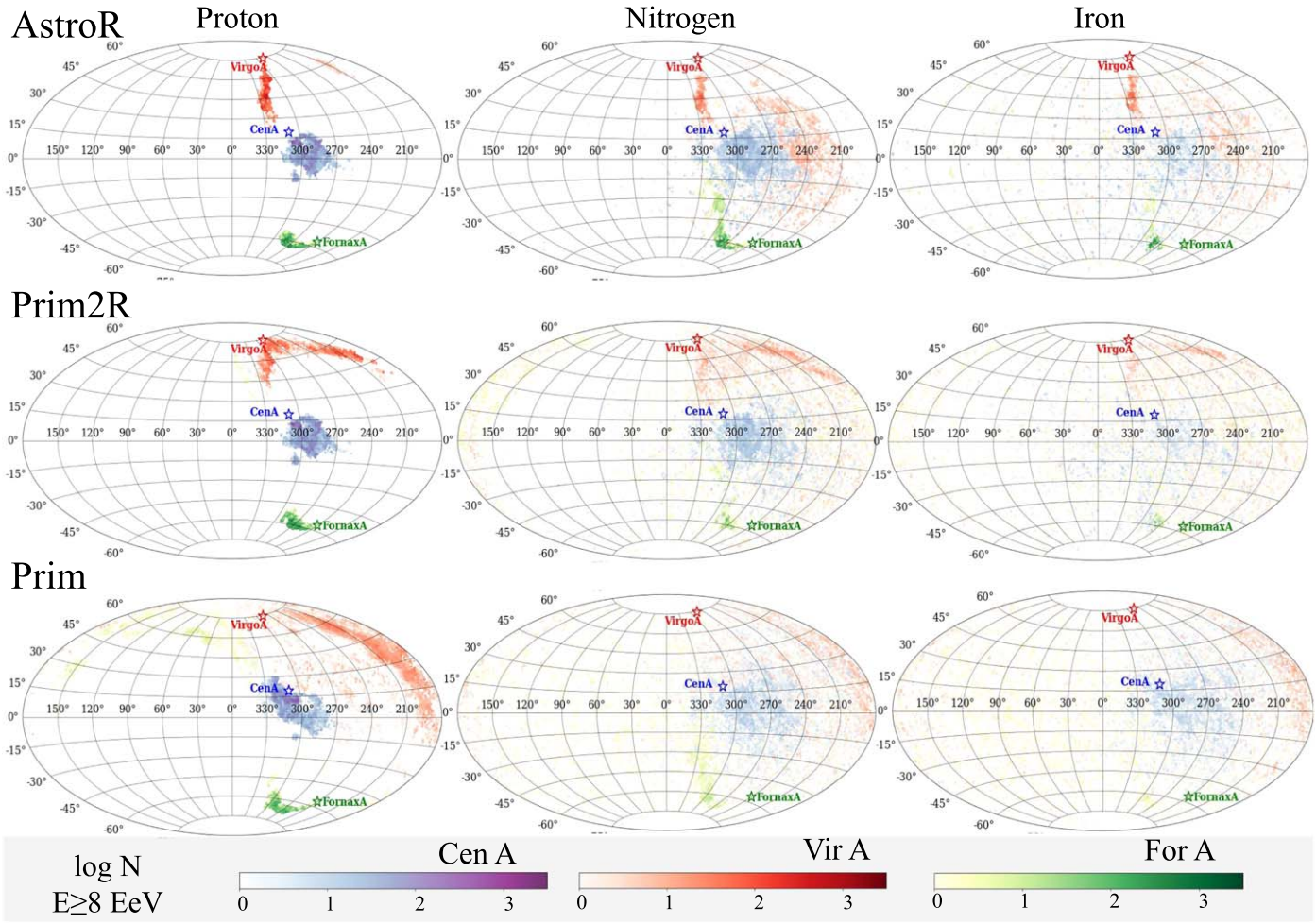

Figure 3. Sky maps in Galactic coordinates and Aitoff projections of all simulated events that arrived at Earth with energy above 8 EeV. Each line in the figure shows one of the EGMF models considered here. Each column in the figure shows a different nucleus leaving the source: proton, nitrogen, and iron nuclei. Note that in each column of the figure, all nucleus fragments on the way to Earth are shown as arriving at Earth although only proton, nitrogen, or iron nuclei left the source. The three sources are shown as blue, red, and green stars for Cen A, Vir A, and For A, respectively. The flux of events follows the same color coding, each color representing only the events generated in the respective source.

and so, the mean free path for proton–proton interactions in this medium is of the order of 1 Gpc.

The Galactic magnetic field (GMF) is known to have a large effect on the arrival direction of UHECRs (Farrar et al. 2013; Erdmann et al. 2016). For all plots and analyses in this paper, the most updated GMF model of Jansson & Farrar (2012, JF12) was used. The regular and random components were taken into account. This model includes the analysis of the WMAP7 Galactic Synchrotron Emission map and 40,000 extragalactic rotation measures. Because the Milky Way is significantly smaller than the closest source distance considered here ($D^{\mathrm{CenA}} = 3.8$ Mpc), UHECR energy losses inside our galaxy were ignored, allowing the net effect of the GMF in the arrival direction of UHECRs to be accounted for using parameterizations (Bretz et al. 2014).

The extragalactic magnetic field (EGMF) is also known to have a large effect on the arrival directions of UHECRs (Sigl et al. 2004). The EGMF intensity can be inferred using several techniques, including gamma-ray energy spectrum modulations of distant sources, Faraday rotation in the polarized radio emission from distant sources, and properties of the cosmic microwave background radiation (Kronberg 1994; Durrer & Neronov 2013; Subramanian 2016). Because these are integrated measurements that depend mainly on the perpendicular component of the field, nothing can be extracted about the EGMF topology from these data (Widrow et al. 2012). Given the uncertainties, simple cellular structure EGMF models (Tanco 2001), based on cosmological arguments of seed fields (Durrer & Neronov 2013), with $\sim 10^{-9}$ G intensity and ∼Mpc correlation length, have been widely used in UHECR propagation studies (Waxman & Miralda-Escudé 1996; Aloisio & Berezinsky 2004; Batista & Sigl 2014). A reference cellular EGMF characterized by cells with 0.37 Mpc size in which the field has random orientation and intensity given by a Kolmogorov spectrum with rms 3 nG was used in some studies below for comparison.

Structured models of the local EGMF with voids and filaments have long been proposed (Ryu et al. 2008; Cho & Ryu 2009). It has been shown that the structure of the EGMF leads to large deflections (>90° below the GZK limit) in the arrival directions of particles generated in local sources (Tanco 1998; Das et al. 2008). In this paper, the most updated simulation of the local EGMF is used (Hackstein et al. 2018). This reference calculates the local EGMF structure from two fundamental hypotheses, named primordial and astrophysical. The primordial models start with a nonnegligible EGMF at $z = 60$. The astrophysical one was modeled as impulsive thermal and magnetic feedback in halos

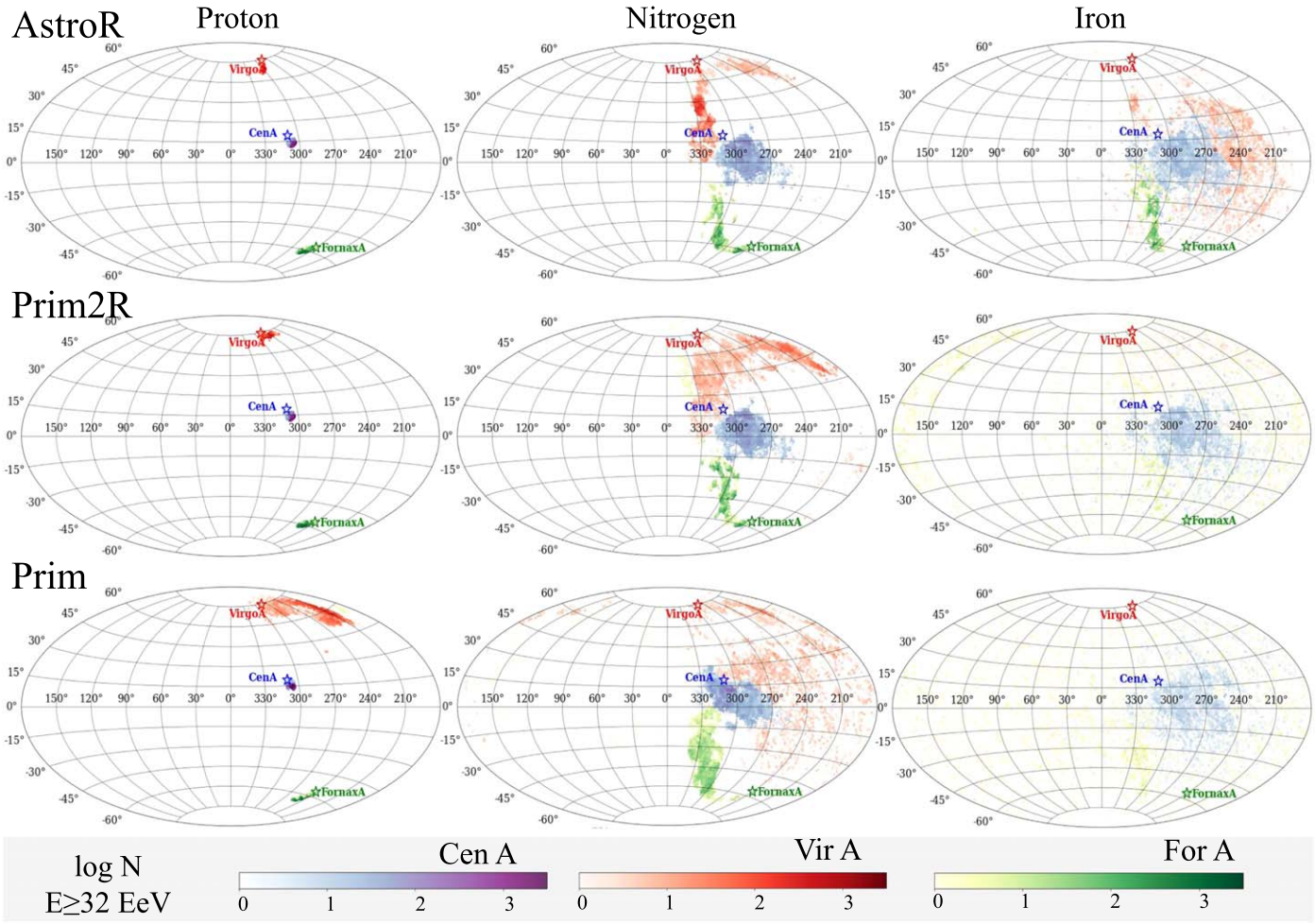

Figure 4. Sky maps in Galactic coordinates and Aitoff projections of all simulated events which arrived at Earth with energy above 32 EeV. Each line in the figure shows one of the EGMF models considered here. Each column in the figure shows a different nucleus leaving the source: proton, nitrogen, and iron nuclei. Note that in each column of the figure, all nucleus fragments on the way to Earth are shown as arriving at Earth although only proton, nitrogen, or iron nuclei left the source. The three sources are shown as blue, red, and green stars for Cen A, Vir A, and For A, respectively. The flux of events follows the same color coding, each color representing only the events generated in the respective source.

starting with a uniform lower magnetic field level of 10^{-20} G at $z = 60$. Magnetohydrodynamical simulations evolve the EGMF to the present time taking into consideration several constraints in a ΛCDM universe. In this paper, three EGMF models from Hackstein et al. (2018) are used, covering the widest range of field intensity and level of structure: AstrophysicalR (AstroR), Primordial2R (Prim2R), and Primordial (Prim), where Prim starts with a uniform 0.1 nG intensity field, while Prim2R starts with a power-law distribution of spectral index −3 and $B_{\rm rms} = 1$ nG. Maps of the intensity of these fields with the position of the sources studied here are shown in Hackstein et al. (2018) and de Oliveira & de Souza (2021).

3. Results: Arrival Directions of UHECRs from Cen A, Vir A, and For A

Figure 1 shows the relative flux of UHECRs in small portions of the sky around Cen A, Vir A, and For A. Each line in the figure shows one EGMF model: AstroR, Prim2R, and Prim. Each column in the figure shows the results for one source: Cen A, Vir A, and For A. Particles were tracked from the source (center of the map) until they reach a sphere with radius equal to the distance from the source to Earth. The maps show the arrival position of all particles in this sphere. The blue circle shows the position of Earth. The color code in the maps shows the relative flux of UHECRs. All nuclei are considered to leave the source with equal flux. Similar maps, leading to the same conclusions, with only protons and only iron nuclei leaving the source, are shown in Appendix B. There are clear regions with enhanced and suppressed flux for each source and EGMF model. The effect of the structure of the EGMF is very evident.

The relative flux of UHECRs arriving at Earth from each source is strongly affected by the local structure of the EGMF. The flux at Earth's position is not greatly affected by the EGMF choice when Cen A is considered. Earth is in a flux-suppressed position to receive UHECRs from Vir A. The EGMF structure diverts UHECRs from Vir A, causing a lack of events from its direction. The reduction of events from Vir A is very clear in Figure 1 for the Prim2R and Prim models, and despite being less visible, it is also present for the AstroR model. Earth is in a favored position to receive UHECRs from For A. The EGMF structure focuses UHECRs from For A in the direction of Earth, as can be clearly seen in the maps.

Figure 2 shows the angular distribution of events in relation to the source direction. Each line in the figure shows one EGMF model: AstroR, Prim2R, and Prim. Each column in the

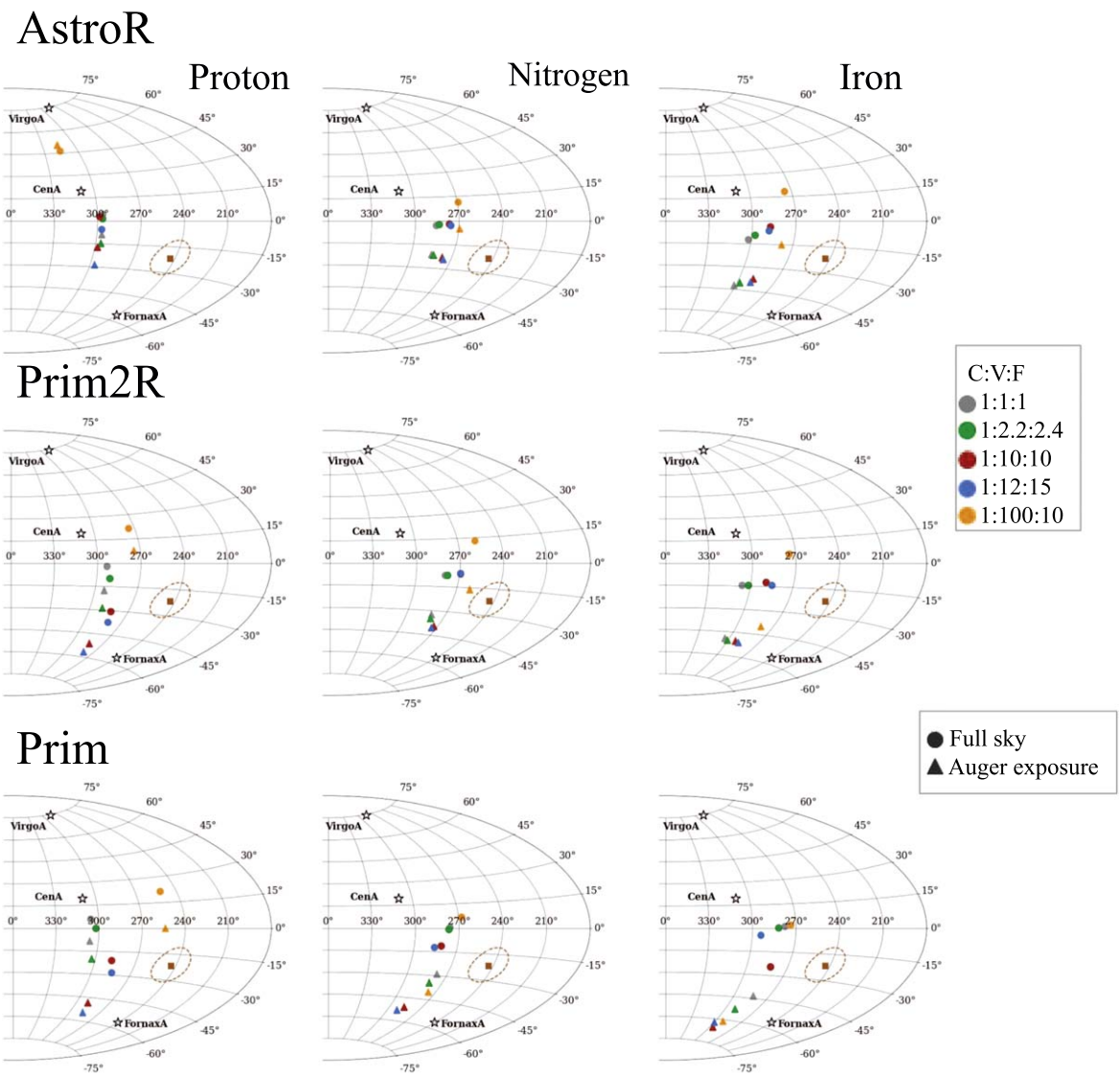

Figure 5. Sky maps in Galactic coordinates and Aitoff projections showing the dipole direction for the simulated events arriving at Earth with energy above 8 EeV. Each line in the figure shows one of the EGMF models considered here. Each column in the figure shows a different nucleus leaving the source: proton, nitrogen, and iron nuclei. Note that in each column of the figure, all nucleus fragments on the way to Earth are shown as arriving at Earth although only proton, nitrogen, or iron nuclei left the source. The three sources are shown as stars. The brown square shows the direction of the dipole measured by the Pierre Auger Observatory, and the dashed brown line shows its 1σ uncertainty. Colored circles show the direction of the dipoles calculated with the simulated events from Cen A, Vir A, and For A. Each color corresponds to a relation of the flux emitted by Cen A:Vir A:For A (C:V:F) as given in the legend.

figure shows a different nucleus leaving the source: proton, nitrogen, and iron nuclei, representing light, intermediate, and heavy composition leaving the sources. Similar plots, leading to the same conclusions for helium and silicon nuclei, are shown in Appendix B. Note that in each column of the figure, all nucleus fragments on their way to Earth are shown as arriving at Earth although only proton, nitrogen, or iron nuclei left the source. The three sources are differentiated by color: blue, red, and green for Cen A, Vir A, and For A, respectively. The sources are considered to output the same UHECR flux. Events deviate by large angles ($\sim 20^{\circ}$) from the source direction even for the nearest source (Cen A). The average deflection depends on the charge of the nuclei leaving the source, being smaller for protons and resulting in an almost uniform distribution for iron nuclei.

The structure of the EGMF interferes clearly with the flux received from each source. For a relatively weak and less structured field (AstroR), the relative number of events arriving at Earth from each source is in a good approximation determined only by the geometric effect. However, the field structure becomes dominant for a stronger and structured EGMF (Prim and PrimR). Note in Figure 2 the larger number of events arriving at Earth from For A than from Vir A when iron nuclei are simulated (right column). If only the geometric effect given by distance under isotropic emission is considered, the flux arriving at Earth from For A would be 1.3 times smaller than the flux from Vir A. When the effect of the EGMF on Prim2R (Prim) is taken into account, the flux arriving at Earth from For A is 38 (443) times larger than the flux from Vir A.

3.1. The Dipole

The Pierre Auger Collaboration published a multipole analysis of the arrival directions of detected events in which a dipole signal was detected (The Pierre Auger Collaboration 2017, 2018b, 2021). In this analysis, the data set was divided into five energy bins: $\geqslant 8$,

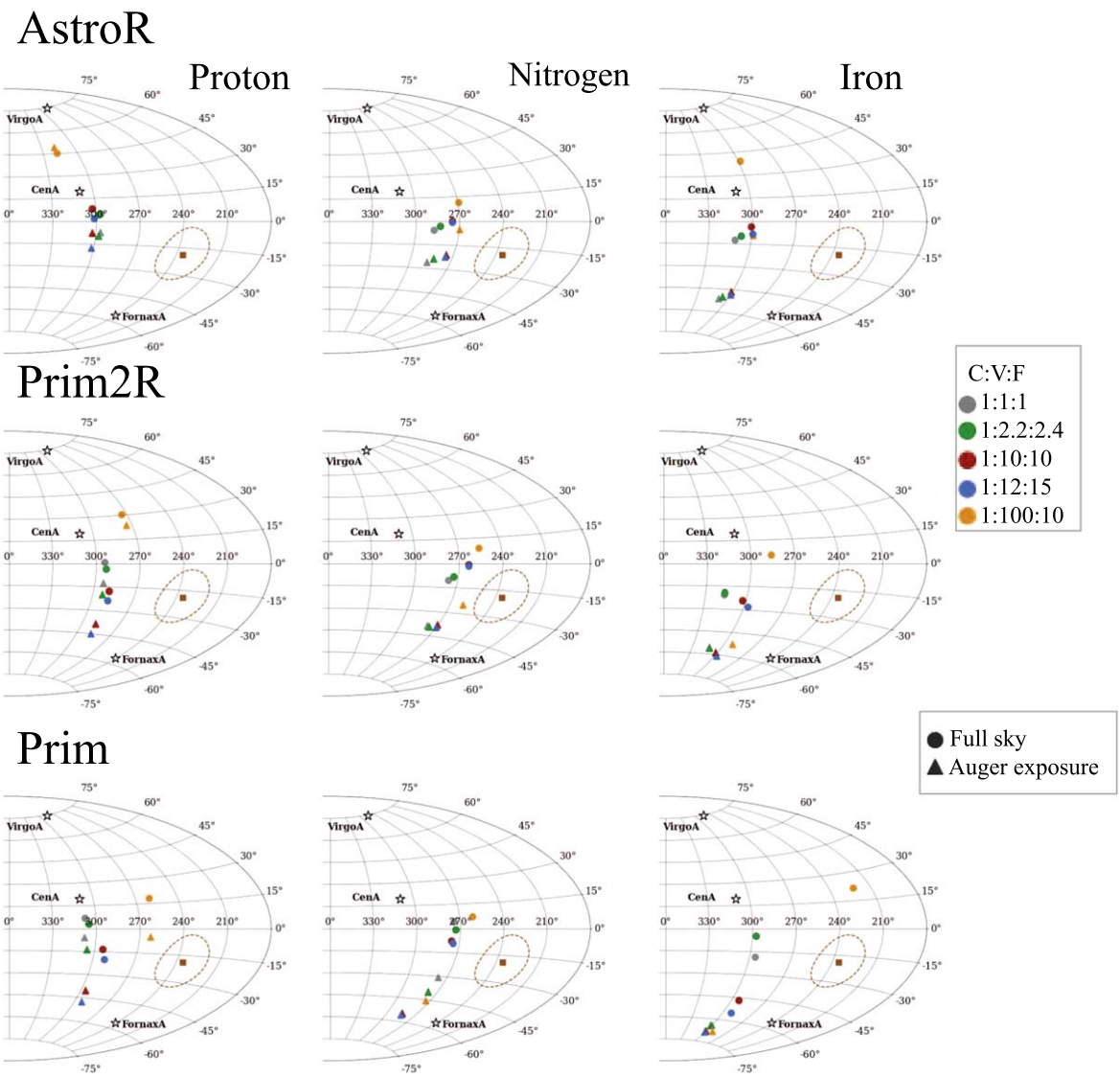

Figure 6. Sky maps in Galactic coordinates and Aitoff projections showing the dipole direction for the simulated events arriving at Earth with energy between 8 and 16 EeV. Each line in the figure shows one of the EGMF models considered here. Each column in the figure shows a different nucleus leaving the source: proton, nitrogen, and iron nuclei. Note that in each column of the figure, all nucleus fragments on the way to Earth are shown as arriving at Earth although only proton, nitrogen, or iron nuclei left the source. The three sources are shown as stars. The brown square shows the direction of the dipole measured by the Pierre Auger Observatory, and the dashed brown line shows its 1σ uncertainty. Colored circles show the direction of the dipoles calculated with the simulated events from Cen A, Vir A, and For A. Each color corresponds to a relation of the flux emitted by Cen A:Vir A:For A (C:V:F) as given in the legend.

4–8, 8–16, 16–32, and $\geqslant$32 EeV. For each energy bin, a dipole was detected at a given direction and amplitude (see Table 1 of The Pierre Auger Collaboration 2021). The p-values under the null hypothesis of isotropy for the first-harmonic modulation in R.A. are 5.1×10^{-11}, 0.14, 3.1×10^{-7}, 7.5×10^{-4}, and 0.01 respectively for the energy bins.

Recent works have shown the importance of local sources in the determination of the dipole direction (Lang et al. 2021). In this section, the dipole directions for the same energy bins considered in the analysis done by the Pierre Auger Collaboration are calculated with the events arriving at Earth from Cen A, Vir A, and For A according to the simulations explained above. The dipole directions generated by the arrival directions of UHECRs simulated from these three sources are compared with the measurement done by the Pierre Auger Observatory. The calculation of the dipole direction with only three sources is a simplification because other sources certainly influence the dipole direction as well. The idea is to test how dominant the influence is of these three sources in the direction of the dipole by ignoring the contribution of other sources. It is expected that nearby sources contribute more significantly to the flux at the highest energies because of the Greisen, Zatsepin & Kuz'min (GZK) suppression (Greisen 1966; Zatsepin & Kuz'min 1966).

Figures 3 and 4 show the arrival directions of the simulated events that arrived at Earth with energies above 8 and 32 EeV, respectively. Each line in the figures refers to one of the EGMF models considered here. Each column in the figures shows a different nucleus leaving the source: proton, nitrogen, and iron nuclei. Similar plots, leading to the same conclusions for helium and silicon nuclei, are shown in Appendix B. Note that in each column of the figure, all nucleus fragments on the way to Earth are shown as arriving at Earth although only proton, nitrogen, or iron nuclei left the source. The three sources are shown as blue, red, and green stars for Cen A, Vir A, and For A, respectively. The flux of events follows the same color

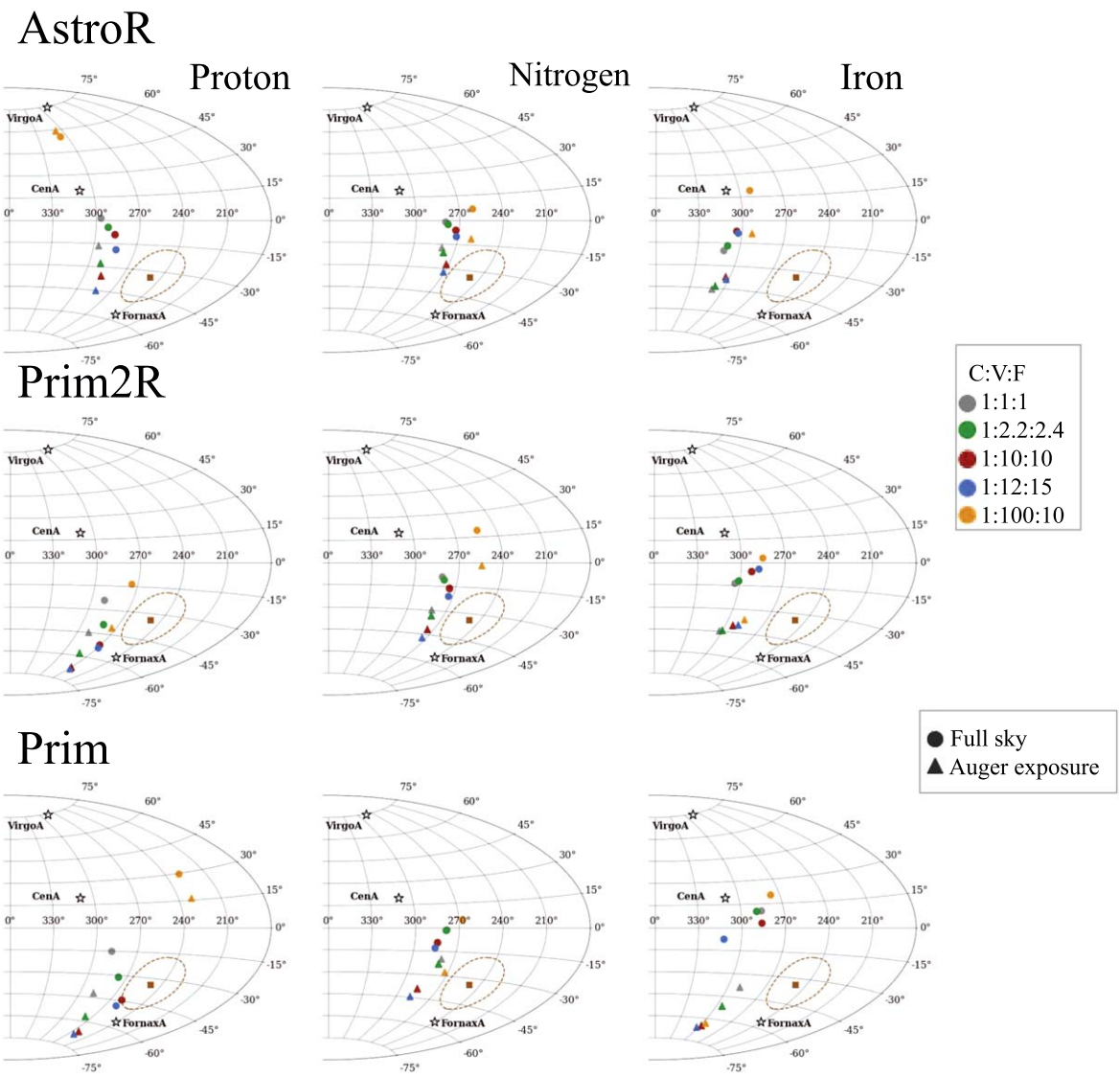

Figure 7. Sky maps in Galactic coordinates and Aitoff projections showing the dipole direction for the simulated events arriving at Earth with energy between 16 and 32 EeV. Each line in the figure shows one of the EGMF models considered here. Each column in the figure shows a different nucleus leaving the source: proton, nitrogen, and iron nuclei. Note that in each column of the figure, all nucleus fragments on the way to Earth are shown as arriving at Earth when only proton, nitrogen, or iron nuclei left the source. The three sources are shown as stars. The brown square shows the direction of the dipole measured by the Pierre Auger Observatory, and the dashed brown line shows its 1σ uncertainty. Colored circles show the direction of the dipoles calculated with the simulated events from Cen A, Vir A, and For A. Each color corresponds to a relation of the flux emitted by Cen A:Vir A:For A (C:V:F) as given in the legend.

coding, each color representing only the events generated in the respective source. The importance of the structure of the local EGMF is evident in many ways.

The overall conclusions in Figures 3 and 4 are the same for the two energy ranges above 8 and 32 EeV with the expected caveat that lower-energy events are more spread out. Protons leaving all three sources (first column) suffer a negligible deflection in the AstroR and Prim2R EGMF models. However, protons leaving Vir A deviate in the Prim EGMF model by large angles, thus arriving at Earth with directions pointing several degrees away from Vir A. Note the large number of events along longitude 210° crossing latitude 60° in the panel in the first column and third line. This enhancement is also evident in Figure 2. Nitrogen (second column) and iron nuclei (third column) leaving Vir A are largely deviated, arriving at Earth with directions corresponding to large portions of the right hemisphere of the plots for all EGMF models (all lines). It is interesting to note that this region presents an event excess in the data from the Pierre Auger Observatory (Figure 4 of The Pierre Auger Collaboration 2018b). Nitrogen and iron nuclei leaving For A (green) produce events arriving at Earth with directions concentrated in the latitude range 300°–330° for all EGMF models. The anisotropic effect in the arrival directions of UHECR caused by the structure of the EGMF has a large impact on the estimate of the dipole direction.

The dipole direction was calculated using the events arriving at Earth from Cen A, Vir A, and For A with energy $\geqslant$8, 8–16, 16–32, and $\geqslant$32 EeV for several cases (see Appendix C). The calculation was done (a) for each EGMF model, (b) for each nucleus type leaving the source, (c) for a set of relative output flux for each source, and (d) full-sky or Auger exposure. Figures 5, 6, 7, and 8 show the calculated directions of the dipole using the simulated events in comparison to the direction of the dipole measured by the Pierre Auger Observatory for the same energy bins. The brown square shows the direction of the dipole measured by the Pierre Auger

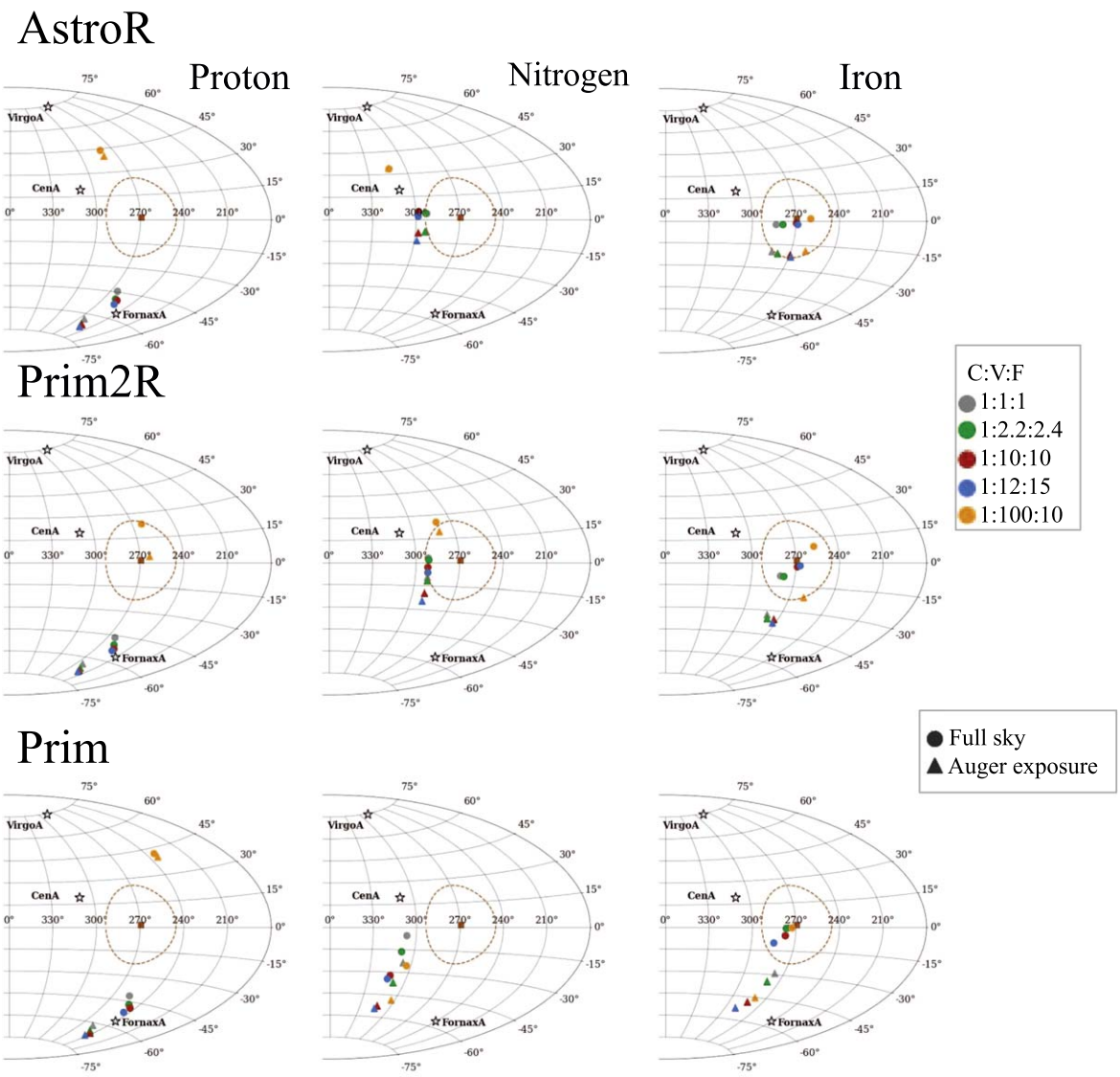

Figure 8. Sky maps in Galactic coordinates and Aitoff projections showing the dipole direction for the simulated events arriving at Earth with energy above 32 EeV. Each line in the figure shows one of the EGMF models considered here. Each column in the figure shows a different nucleus leaving the source: proton, nitrogen, and iron nuclei. Note that in each column of the figure, all nucleus fragments on the way to Earth are shown as arriving at Earth although only proton, nitrogen, or iron nuclei left the source. The three sources are shown as stars. The brown square shows the direction of the dipole measured by the Pierre Auger Observatory, and the dashed brown line shows its 1σ uncertainty. Colored circles show the direction of the dipoles calculated with the simulated events from Cen A, Vir A, and For A. Each color corresponds to a relation of the flux emitted by Cen A:Vir A:For A (C:V:F) as given in the legend.

Observatory, and the dashed brown line shows its 1σ uncertainty. The 1σ uncertainty of the simulated events for the same statistics used by the Pierre Auger Observatory is about 2° and therefore was omitted from the plots for the sake of clarity. Proton, nitrogen, and iron nuclei leaving the source are shown in the figures as representations of light, intermediate, and heavy composition leaving the sources. Note that in each column of the figure, all nucleus fragments on the way to Earth are shown as arriving at Earth although only proton, nitrogen, or iron nuclei left the source. Similar plots, leading to the same conclusions for helium and silicon nuclei, are shown in Appendix B. Colored circles show the direction of the dipoles calculated with the simulated events. Each color corresponds to a relation of the flux emitted by Cen A:Vir A:For A. Five examples of the relation between the fluxes were chosen. Because no other source is considered in this study, only the relative flux is important. Three arbitrary, simplistic, and extreme cases of 1:1:1, 1:10:10, and 1:100:10 were calculated. Two scientifically motivated cases are also shown: 1:2.2:2.4 and 1:12:15. The UHECR luminosity of AGNs is considered to be directly related to the mechanical jet power (Willott et al. 1999). A possible relation between radio luminosity and UHECR flux has been explored in the literature (Eichmann et al. 2018). Using the radio luminosity at frequency $\nu = 1.1$ GHz given in Section 2, the 1:2.2:2.4 ratio is found. Another possible relation between the jet power and X-ray cavity properties present in hot gaseous halos of radio galaxies has been proposed in Godfrey & Shabala (2015). Using the X-ray cavity properties of each source considered here (Godfrey & Shabala 2015), the 1:12:15 ratio can be calculated. It is not in the scope of this paper to discuss the different estimations of UHECR luminosity for the source. For this reason, a large set of possibilities is used in the hopes of bracketing the true unknown value.

Figures 5, 6, and 7 show that the dipole direction measured by the Pierre Auger Observatory in the energy bins $\geqslant$8, 8–16,

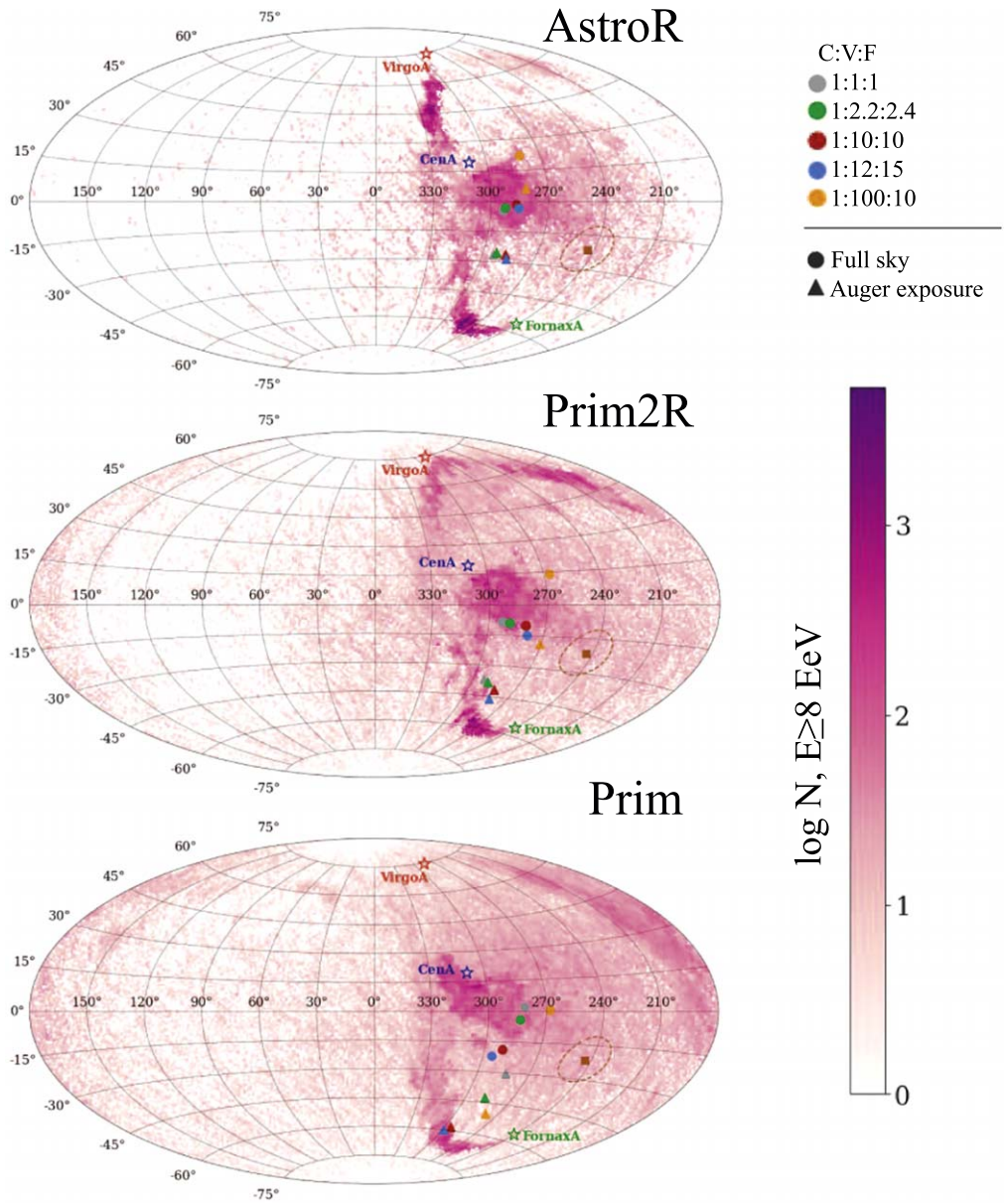

Figure 9. Sky maps in Galactic coordinates and Aitoff projections showing the dipole direction for the simulated events with energy above 8 EeV. Each line in the figure shows one of the EGMF models considered here. The three sources are shown as stars. The brown square shows the direction of the dipole measured by the Pierre Auger Observatory, and the dashed brown line shows its 1σ uncertainty. All primaries (H+He+N+Si+Fe) are plotted with equal fluxes leaving the sources. Colored circles show the direction of the dipoles calculated with the simulated events from Cen A, Vir A, and For A. Each color corresponds to a relation of the flux emitted by Cen A:Vir A:For A (C:V:F) as given in the legend.

16–32 EeV cannot be explained only with the three local sources Cen A, Vir A, and For A and any combination of nuclei leaving the sources independent of the EGMF model, be it AstroR, Prim2R, or Prim, and independent of the ratio between the flux of the sources. Figure 8 shows that the dipole direction measured by the Pierre Auger Observatory at energies above 32 EeV can be explained only with the three local sources Cen A, Vir A, and For A if they inject heavy nuclei independent of the EGMF model, be it AstroR, Prim2R, or Prim, and independent of the ratio between the fluxes of the sources. The dipole amplitude cannot be calculated only with three sources because other sources, even if contributing isotropically to the arrival direction, would decrease the dipole amplitude of nearby sources. For this reason, no comparison between the dipole amplitude measured by the Pierre Auger Observatory and the simulated amplitude with the three sources is shown.

Another illustrative view of the contribution of each source is shown in Figures 9 and 10 in which all nuclei (H+He+N+Si +Fe) are shown with equal fluxes leaving the sources together with the corresponding dipole directions. Other elements of these figures are the same as in Figures 5 and 8.

3.2. The Hotspots

The Pierre Auger Observatory has identified two regions with an excess of events in comparison to simulations of the isotropic sky for events with energy above 60 EeV (The Pierre Auger Collaboration 2018b). The exact position of the center of these regions, named here hotspots 1 and 2 (HS1 and HS2),

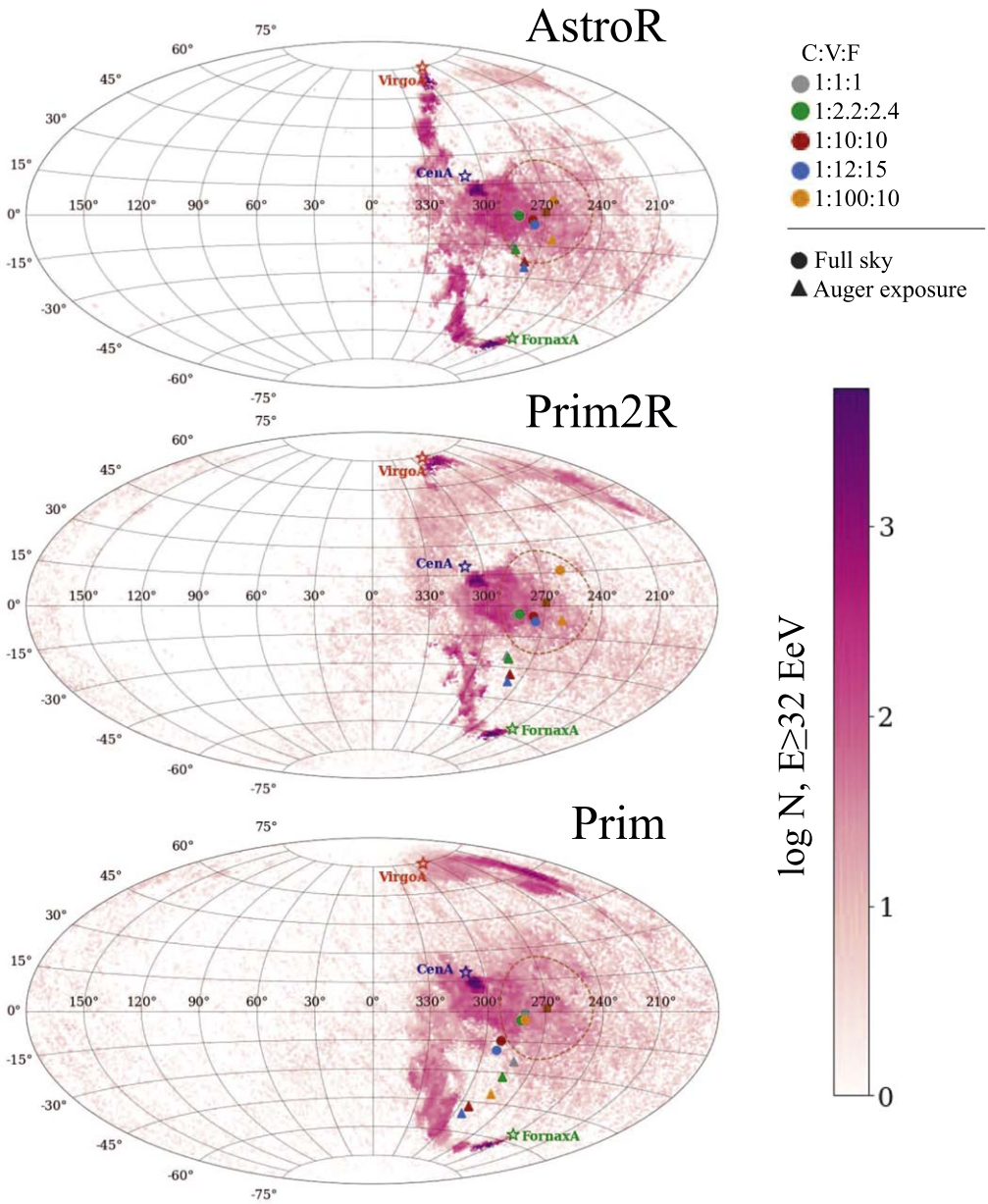

Figure 10. Sky maps in Galactic coordinates and Aitoff projections showing the dipole direction for the simulated events that arrived at Earth with energy above 32 EeV. Each line in the figure shows one of the EGMF models considered here. The three sources are shown as stars. The brown square shows the direction of the dipole measured by the Pierre Auger Observatory, and the dashed brown line shows its 1σ uncertainty. All primaries (H+He+N+Si+Fe) are plotted with equal fluxes leaving the sources. Colored circles show the direction of the dipoles. Each color corresponds to a relation of the flux emitted by Cen A:Vir A:For A (C:V:F) as given in the legend.

was not published by the Pierre Auger Collaboration. From the published maps, the hotspot position was estimated to be ($l = 305°$, $b = 25°$) (HS1) and ($l = 290°$, $b = -70°$) (HS2). The Telescope Array Observatory identified a cluster of events, named here hotspot 3 (HS3), using 20° radius circles of events with energy above 57 EeV. The hotspot has a Li–Ma statistical significance of 5.1σ and is centered around ($l = 146.^{\circ}7$, $b = 43.^{\circ}2$) in Galactic coordinates. In this section, the contribution of Cen A, Vir A, and For A to the hotspots under a structured EGMF is investigated.

Figure 11 shows the three hotspot regions encircled by black solid lines. It also shows the arrival directions of the simulated events arriving at Earth with energies above 60 EeV. HS1 and HS2 were detected for events with energy above 60 EeV, and HS3 was detected for events with energies above 57 EeV. However, the energy reconstruction of both the Pierre Auger and Telescope Array Observatories are known to have systematic uncertainties of the order of 14% and 21%, respectively (The Pierre Auger & Telescope Array Collaborations 2019). For this reason, the small difference between the energies above which the hotspots were detected, of the order of 5%, is ignored in the following studies, and all simulated events with energies above 60 EeV are taken into consideration.

Each line in Figure 11 shows one of the EGMF models considered here. Each column shows a different nucleus leaving the source: proton, nitrogen, and iron. Note that in each column of the figure, all nucleus fragments on the way to Earth are shown as arriving at Earth although only proton, nitrogen,

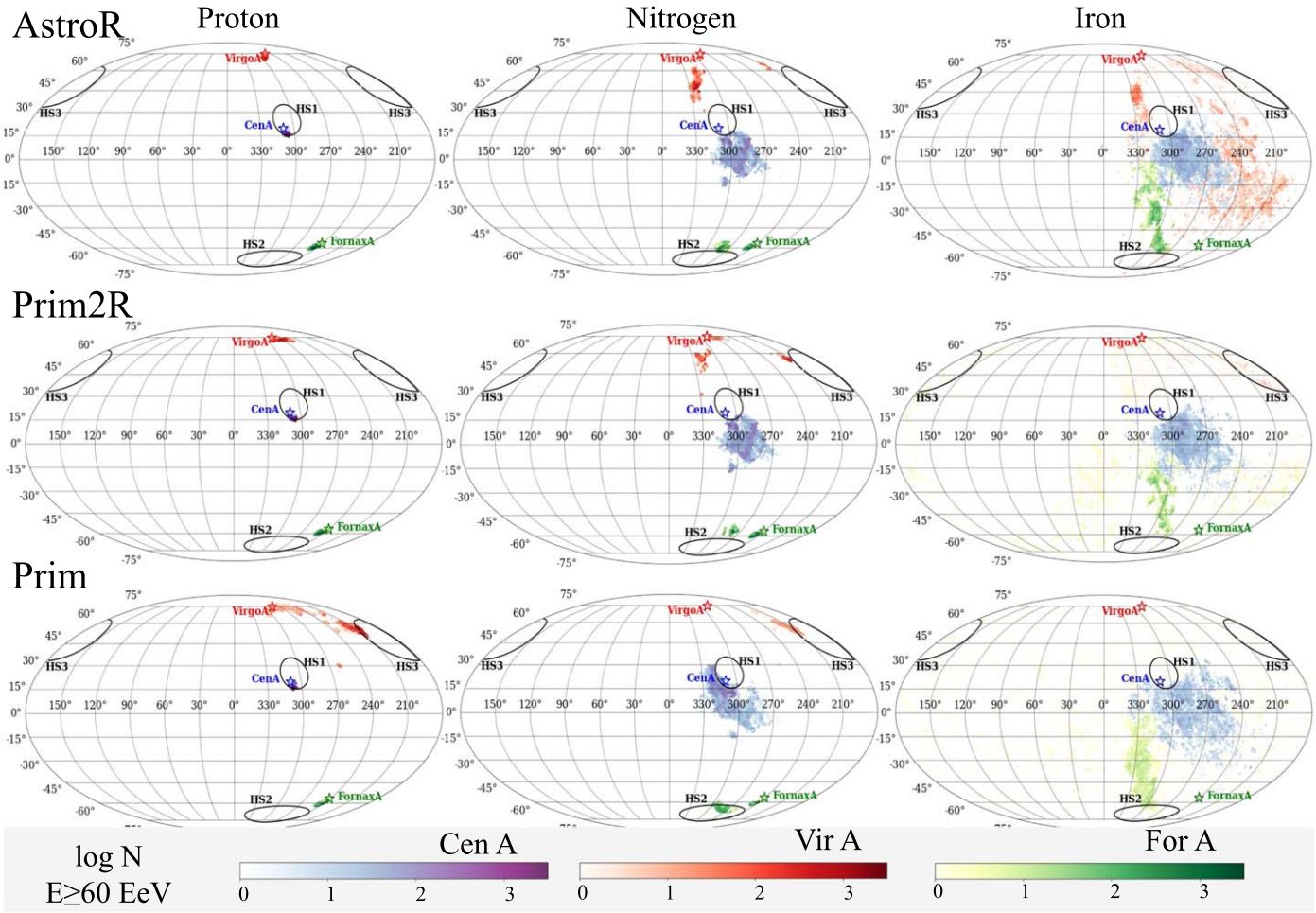

Figure 11. Sky maps in Galactic coordinates and Mollweide projections of all simulated events that arrived at Earth with energy above 60 EeV. Each line in the figure shows one of the EGMF models considered here. Each column in the figure shows a different nucleus leaving the source: proton, nitrogen, and iron nuclei. Note that in each column of the figure, all nucleus fragments on the way to Earth are shown as arriving at Earth although only proton, nitrogen, or iron nuclei left the source. The three sources are shown as blue, red, and green stars for Cen A, Vir A, and For A, respectively. The flux of events follows the same color coding, each color representing only the events generated in the respective source. The three hotspot regions are encircled by black solid lines.

or iron nuclei left the source. Similar plots, leading to the same conclusions for helium and silicon nuclei, are shown in Appendix B. The three source positions are shown by colored stars: blue, red, and green for Cen A, Vir A, and For A, respectively. The flux of events follows the same color coding, each color representing only the events generated in the respective source. The importance of the structure of the local EGMF is evident in many ways.

Protons leaving all three sources (first column) suffer a negligible deflection in the AstroR and Prim2R EGMF models. However, protons leaving Vir A deviate in the Prim EGMF model, accumulating an excess of events in the HS3 region. Nitrogen nuclei leaving Vir A also deviate in all EGMF models in the direction of the HS3 region, and the Prim2R and Prim EGMF models especially generate a clear accumulation of events in the HS3 region. Iron nuclei leaving Vir A strongly deviate in all EGMF models. Some accumulation is caused in the AstroR model and no high concentration of events are obtained from Prim2R and Prim. Iron nuclei leaving For A accumulate events along the longitude 330°, right above the HS2 region. Nitrogen nuclei accumulate events in the HS2 region for all EGMF models.

Another illustrative view of the correlation between HS1 and Cen A, HS2 and For A, and HS3 and Vir A is shown in Figure 12 in which all primaries (H+He+N+Si+Fe) are plotted with equal fluxes leaving the sources. The Cellular EGMF is included for comparison. The structures caused by the AstroR, Prim2R, and Prim EGMF become more evident in comparison to the Cellular map. Note that a Cellular EGMF gives no contribution to the hotspots. Other elements in this figure are the same as in Figure 11.

4. Conclusion

This paper has two main conclusions as summarized in this section. First, it is shown that the structure of the EGMF dominates the arrival directions of UHECRs from events from nearby sources. Second, evidence is presented that the measured signals of anisotropy (dipole and hotspots) are largely determined by events generated by Cen A, Vir A, and For A.

The overall effect of the structure of the EGMF on the arrival directions of UHECRs that originated from nearby sources is very important. At the highest energies investigated here, the galactic magnetic field has a minor contribution to the highly directional effects presented in this conclusion (Erdmann et al. 2016). Events deviate at large angles even for the closest source (see Figure 2). This conclusion confirms previous works

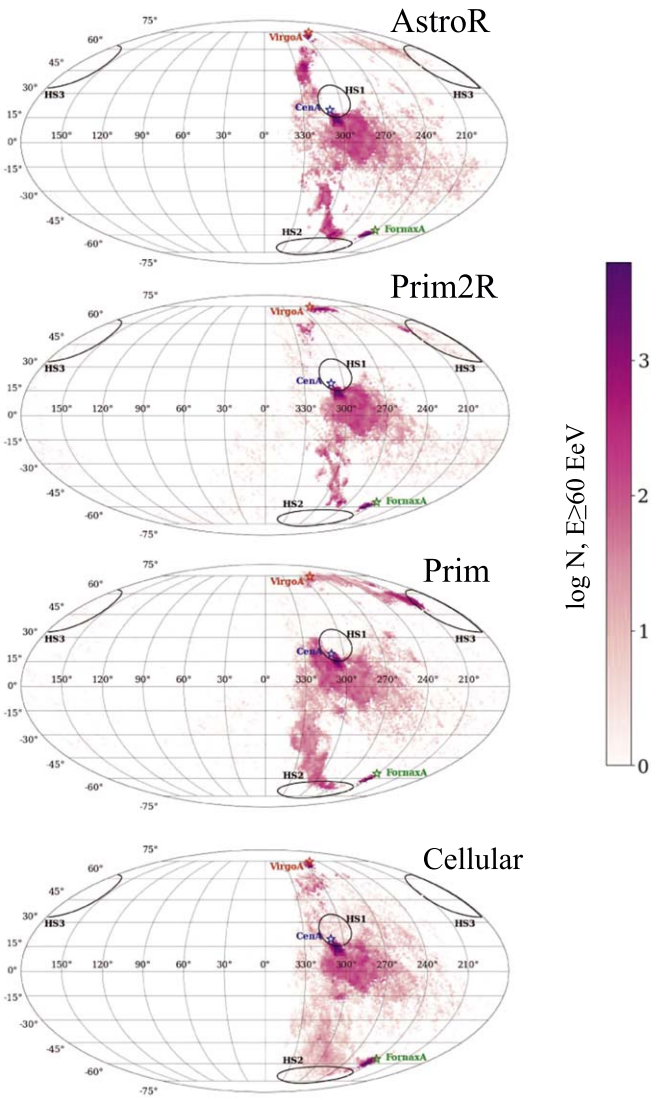

Figure 12. Sky maps in Galactic coordinates and Mollweide projections of all simulated events that arrived at Earth with energy above 60 EeV. Each line in the figure shows one of the EGMF models considered here. The three sources are shown by stars. All primaries (H+He+N+Si+Fe) are plotted with equal fluxes leaving the sources. The three hotspot regions are encircled by black solid lines.

(Lee et al. 1995; Tanco 2001, 1998; Sigl et al. 2003, 2004) with modern tools and EGMF models. It is important to note that these results do not conflict with the finding of Hackstein et al. (2018), in which a continuous source distribution covering a much wider range of distances (up to 100 Mpc) was used. The combination of the two approaches, local point sources and long-range continuous source distribution, is a key aspect to determine the influence on the arrival directions of UHECRs at Earth. According to the results of this paper and also previous calculations (Tanco 2001, 1998), the immersion of the source in localized EGMF sheets and filaments separated by vast voids has important consequences on the propagation of UHECRs. Ding et al. (2021) studied imprints of the local scale structure (LSS) of matter in the UHECR sky. Their fundamental hypothesis is that the sources are distributed according to the LSS, and the EGMF is considered to be a simple cellular type. Concerning the hotspots, they concluded that some excess near the South Galactic Pole seen above 38 EeV could potentially be due to the large-scale distribution of matter rather than individual dominant sources. Differently from Ding et al. (2021), the calculations shown here suggest that the EGMF structure is the dominant aspect. As summarized below, if a structured EGMF is used in the simulation, several measured signals of anisotropy can be reproduced.

The structure of the EGMF is proposed as the reason for the lack of an excess in the data measured by the Pierre Auger Observatory in the direction of Vir A. In agreement with the previous suggestion (Tanco 2001; Dolag et al. 2009), it was shown in Section 3, using the most updated simulation and EGMF models, how the Prim and Prim2R EGMF models create suppression and enhancement regions in the surroundings of the sources. The AstroR EGMF is much less structured than the others, and the effect is less evident. Earth is in a disfavored position to receive UHECRs from Vir A, and the EGMF diverts particles from Vir A away from Earth's direction. Earth is in a favored position to receive UHECRs from For A, and the EGMF focuses particles from For A toward Earth.

The suppression/enhancement or lensing effect of the EGMF has important effects on the direction of the dipolar component of the distribution of the arrival directions. The suppression of Vir A, for instance, moves the dipole direction toward lower latitudes. The dipole direction measured by the Pierre Auger Observatory with energies $\geqslant$8, 8–16, 16–32 EeV cannot be explained only by Cen A, Vir A, and For A independently of nuclei leaving the source and of the structure of the EGMF. The dipole direction measured by the Pierre Auger Observatory with energy above 32 EeV can be explained only by Cen A, Vir A, and For A if a large fraction of the emitted UHECR events are heavy nuclei independently of the structure of the EGMF. This suggests a transition in the predominance from local to distance sources in the dipole signal in the energy range from 8 to 32 EeV.

EGMF lensing effects are a major inducer of hotspots. The HS1 measured by the Pierre Auger Observatory close to the direction of Cen A is probably caused by light primaries produced in Cen A as has been shown previously and confirmed here. The detailed simulations done here show that the arrival directions of protons under the strongest and most structured EGMF model (Prim) are centered still far away ($\sim$10°) from the centroid of HS1. This implies that HS1 cannot be explained only by protons from Cen A. Heavier nuclei from Cen A would not help to populate HS1 because they deviate away from the HS1 direction. It is also shown in Section 3.2 that Vir A does not contribute to HS1 even when the strongest and most structured EGMF model is considered. The calculations also show hints that HS2 can receive a contribution from intermediate nuclei leaving For A independent of the EGMF model considered. The calculations also show that HS3 can receive a contribution from light to intermediate nuclei leaving Vir A if strong and structured EGMF (Prim and Prim2R) are considered. The overall conclusions of this study concerning the hotspots are hints that For A contributes to HS2 and Vir A contributes to HS3, aside from the confirmation that Cen A contributes to HS1.

The Telescope Array Collaboration has suggested that HS3 received a strong contribution from the starburst region M82 (NGC 3034) (The Telescope Array Collaboration 2020). The conclusion of the Telescope Array Collaboration was based on the simulation of a cellular type of EGMF that causes a

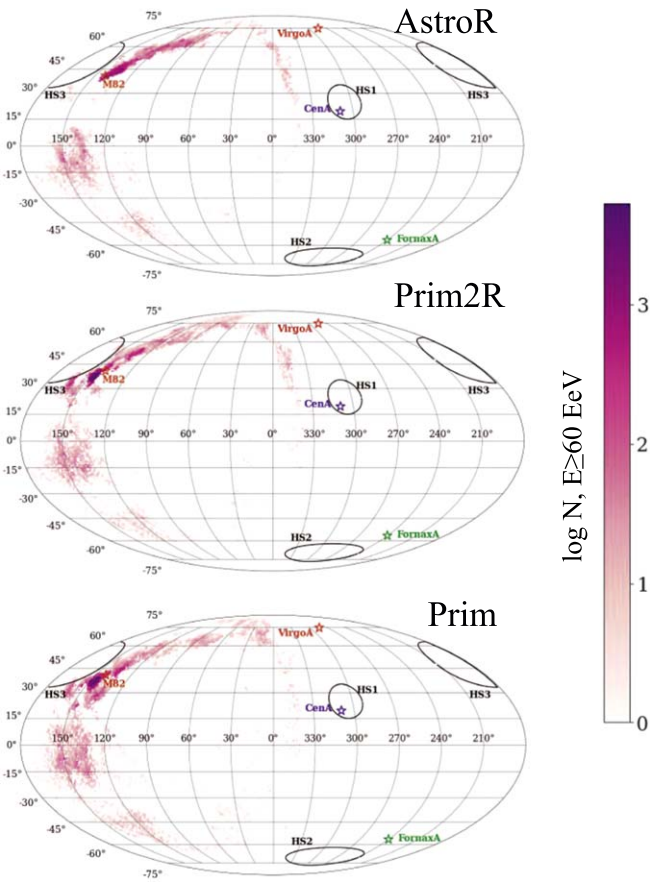

Figure 13. Sky maps in Galactic coordinates and Mollweide projections of all simulated events which arrived at Earth with energy above 60 EeV. Each line in the figure shows one of the EGMF models considered here. The four sources are denoted by stars. All primaries (H+He+N+Si+Fe) are plotted with equal fluxes leaving the sources. The three hotspot regions are encircled by black solid lines. The flux of events arriving at Earth from M82 is shown color-coded according to the legend.

symmetric dispersion of the events around the true source direction. Figure 13 shows events arriving from M82 when the AstroR, Prim2R, and Prim EGMF models are considered. All nuclei (H+He+N+Si+Fe) are shown with equal fluxes leaving the source. According to these simulations, M82 does not contribute to the HS3 independent of the EGMF model and nuclei type. Under structured EGMF models, the events leaving M82 are diverted asymmetrically and away from HS3.

The EGMF lensing effects shown here represent a paradigm shift from the random walk propagation effect of classical UHECR propagation. The lensing effect proposed previously (Lee et al. 1995; Tanco 2001, 1998; Sigl et al. 2003, 2004) and studied here with recent EGMF models and modern propagation codes is shown to be mandatory to interpret the arrival directions measured by the most important observatories. According to the results presented here, the sky map produced by local sources might have a large composition-dependent anisotropy that could be tested by observatories with enhanced capabilities to reconstruct the primary particle type of air showers.

C.O. and V.d.S. acknowledge FAPESP Project 2015/15897-1, 2019/10151-2, and 2020/15453-4. The authors acknowledge the National Laboratory for Scientific Computing (LNCC/MCTI, Brazil) for providing the HPC resources of the SDumont supercomputer (http://sdumont.lncc.br). V.d.S acknowledges CNPq. This study was financed in part by the Coordenação de Aperfeiçoamento de Pessoal de Nível Superior —Brasil (CAPES) - Finance Code 001. The authors thanks Edivaldo Santos Moura and Rogério de Almeida Menezes for useful discussions.

Appendix A
UHECR Emission Model

In this appendix, the UHECR emission model used in this paper is explained. First-order Fermi acceleration is the paradigm for particle acceleration (Kotera & Olinto 2011). Diffusive shock acceleration has been proposed as the main acceleration mechanism in AGN jets (Matthews et al. 2019) leading to a power-law energy spectrum with an index around 2 and a charge-dependent exponential cutoff (Supanitsky & de Souza 2013) that accounts for the limitation in the maximum energy to which a source can accelerate particles:

$$\frac{dN}{dEdt} = L_{CR}E^{-2}\exp(-E/ZR_{\rm cut}), \tag{A1}$$

where $L_{\rm CR}$ is the cosmic-ray luminosity, Z is the particle charge, and $R_{\rm cut}$ is the rigidity cutoff such that $E_{\rm cut} = ZR_{\rm cut}$. The cosmic-ray luminosity of each source and the charge of the particles are the case studies in this paper; therefore, in each study in this work, the values of $L_{\rm CR}$ and Z will be defined. The rigidity cutoff is related to the escape time from the source. From Eichmann et al. (2018) and Eichmann (2019) one can relate $R_{\rm cut}$ to the jet power $Q_{\rm jet}$ by

$$R_{\rm cut} = 5.4 g_{\rm ac}\sqrt{1-g_{\rm cr}}\left(\frac{Q_{\rm jet}}{10^{43}\,{\rm erg\ s^{-1}}}\right)^{1/2}{\rm EV}, \tag{A2}$$

where $g_{\rm ac} = \sqrt{\frac{8\beta_{\rm sh}^2}{f^2\beta_j}}$ depends on the plasma physics details in the acceleration site, with $\beta_{\rm sh}$ the typical shock velocity responsible for the particle acceleration (in speed-of-light units) and β_j the jet velocity, and f providing specific plasma properties, with $1 \leqslant f \leqslant 8$ for shocks with typical geometries and turbulent magnetic fields (Eichmann 2019). The typical velocity of the shock waves $\beta_{\rm sh} = 0.2$ (Matthews et al. 2019) is assumed for the three sources. It is estimated that $\beta_j^{\rm CenA} \sim 0.5$ (Hardcastle et al. 2003), $\beta_j^{\rm VirA} \sim 0.9$–$0.99$ (Hada 2013), and $\beta_j^{\rm ForA} \sim 0.4$–$0.9$ (Maccagni et al. 2020). It is estimated that $Q_{\rm jet}^{\rm CenA} \sim 10^{43}$–$10^{44}$ erg s^{-1} (Yang et al. 2012; Sun et al. 2016), $Q_{\rm jet}^{\rm VirA} \sim 10^{44}$–$10^{45}$ erg s^{-1} (Kino et al. 2013), and, by radio flux arguments, $Q_{\rm jet}^{ForA} \sim Q_{\rm jet}^{\rm VirA}$.

The factor g_{cr} accounts for the relation between the energy stored in hadrons and in the magnetic field in the acceleration region (Pacholczyk 1970) and can be written as

$$g_{\rm cr}^{-1} = 1 + \frac{3}{4}\left(\frac{B}{B_m}\right)^{7/2}, \tag{A3}$$

where B is the magnetic field strength in the acceleration region, and B_m is the magnetic field strength in the minimum energy condition. Using $B_m^{\rm CenA} \sim 30$–$60\ \mu$G (Burns et al. 1983; Kraft et al. 2002; Feigelson et al. 1981), $B^{\rm CenA} = 23\ \mu$G (The H.E.S.S. Collaboration et al. 2020), equipartition for Virgo A (Snios et al. 2019) and Fornax A (Maccagni et al. 2020), $B_m^{\rm VirA} = B^{\rm VirA}$, and

$B_m^{\rm ForA} = B^{\rm ForA}$, it is possible to calculate the maximum rigidity cutoffs $R_{\rm cut}^{\rm CenA} = 10^{18.8}$ V, $R_{\rm cut}^{\rm VirA} = 10^{19.3}$ V, and $R_{\rm cut}^{\rm ForA} = 10^{19.5}$ V. As an upper limit, the rigidity cutoff of M82 is taken as $10^{19.5}$ V.

Appendix B
Other Nuclei

In Section 3, the relative flux of UHECRs around each source is presented only for all nuclei with equal flux. Figures 14 and 15 show the same plots for proton and iron nuclei. Another representation of the enhancement/suppression effect is seen in the angular distributions of events in relation to the source direction. In Section 3, the plots were done for proton, nitrogen, and iron nuclei. Figure 16 shows the equivalent plots for helium and silicon nuclei.

In Sections 3.1 and 3.2, plots for H, N, and Fe nuclei were shown as representations of light, intermediate, and heavy compositions. He and Si nuclei were also simulated. The analysis of these simulations confirms the conclusions elaborated on in the text. He nuclei plots represent the transition from light (H) to intermediate (N) nuclei. Si nuclei plots represent the transition from intermediate (N) to heavy (Fe) nuclei. If the He and Si plots were shown together with those for H, N, and Fe nuclei, the figure would become very busy and the symbol sizes would be very small compared to normal page/screen sizes. For these reasons, the He and Si nuclei plots are presented here in Figures 17–23 for completeness.

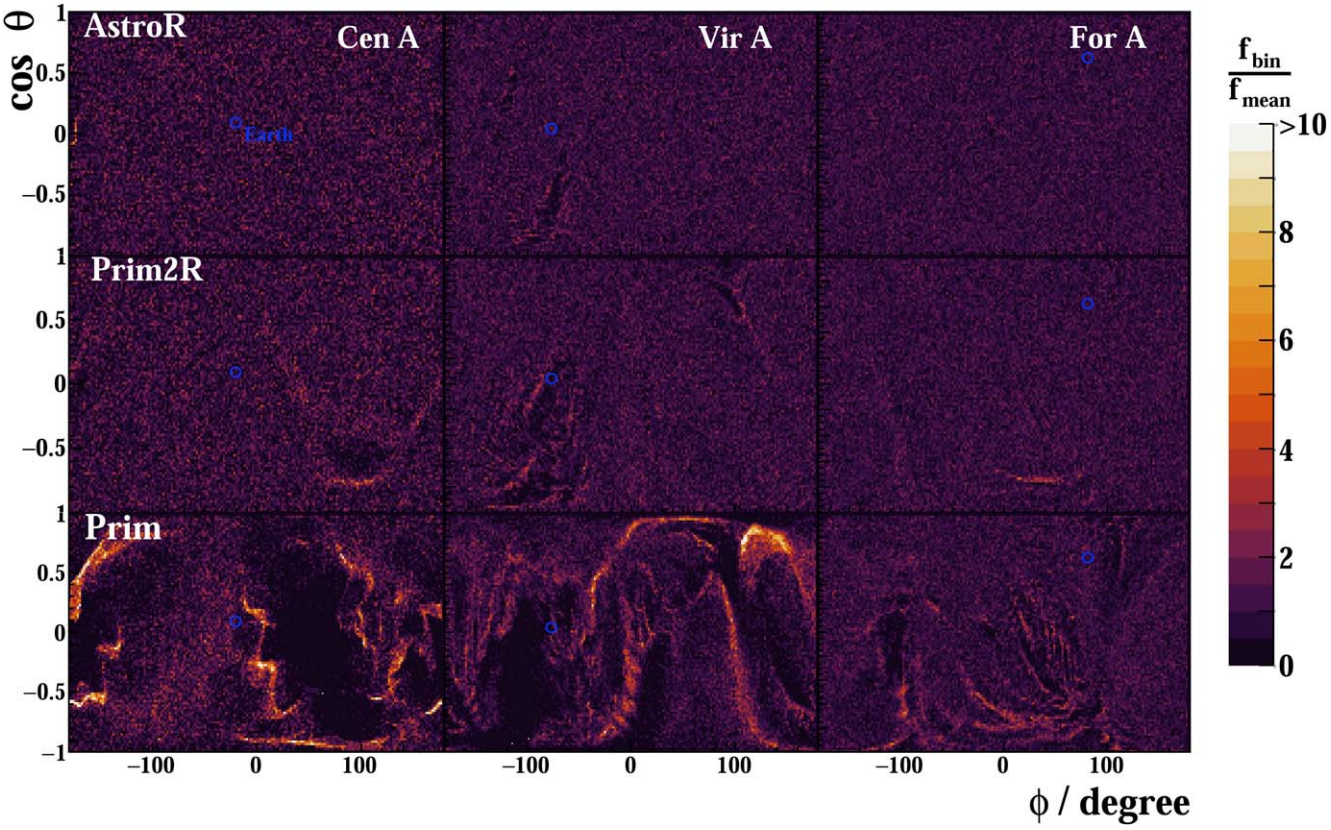

Figure 14. Relative flux of UHECRs around Cen A, Vir A, and For A. Each line in the figure shows one EGMF model: AstroR, Prim2R, and Prim. Each column in the figure shows the results for one source: Cen A, Vir A, and For A. Particles were tracked from the source (center of the map) until they reached a sphere with radius equal to the distance from the source to Earth. The maps show the arrival position of all particles in this sphere. The blue circle shows the position of Earth. The color code in the maps shows the relative flux of UHECRs. Only protons are considered to leave the sources with equal flux.

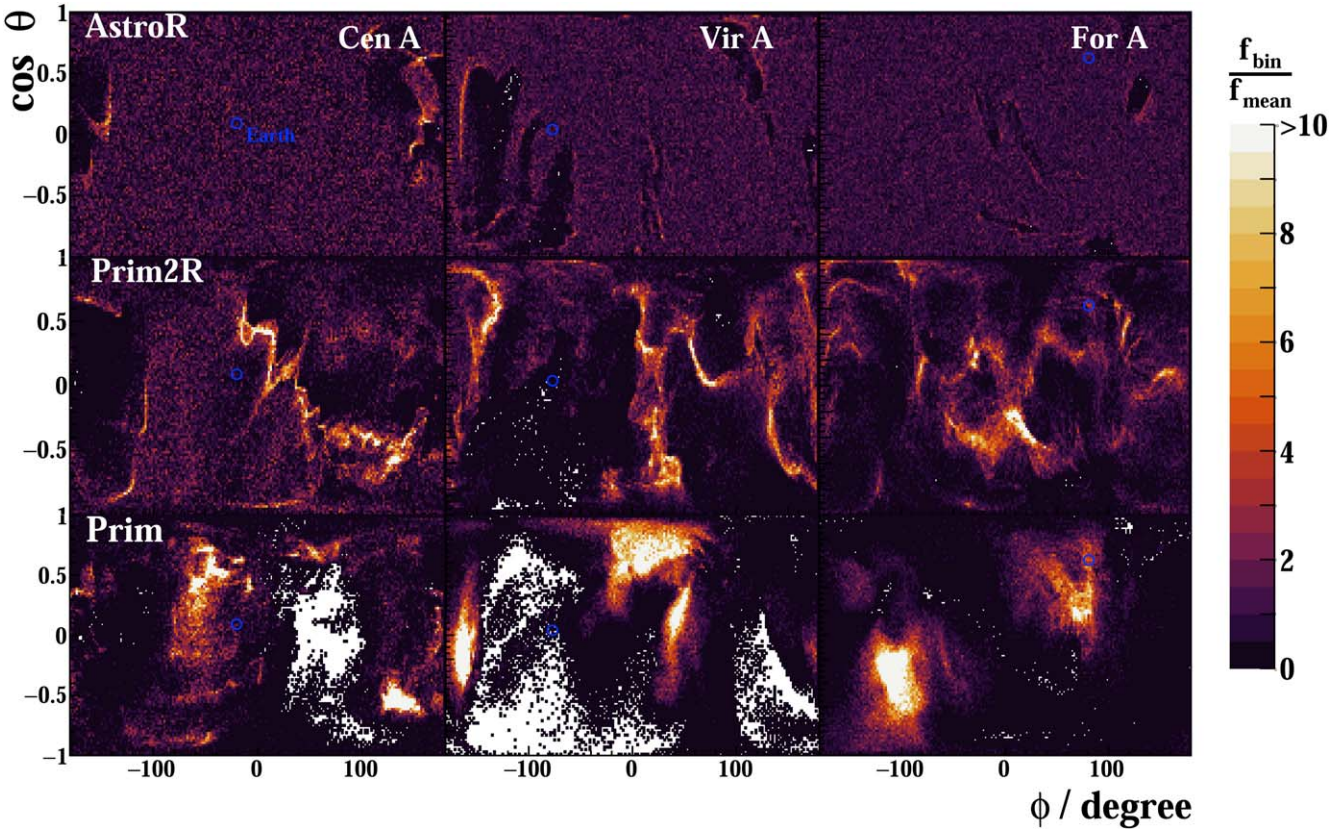

Figure 15. Relative flux of UHECRs around Cen A, Vir A, and For A. Each line in the figure shows one EGMF model: AstroR, Prim2R, and Prim. Each column in the figure shows the results for one source: Cen A, Vir A, and For A. Particles were tracked from the source (center of the map) until they reached a sphere with radius equal to the distance from the source to Earth. The maps show the arrival position of all particles in this sphere. The color code in the maps shows the relative flux of UHECRs. Only iron nuclei are considered to leave the sources with equal flux.

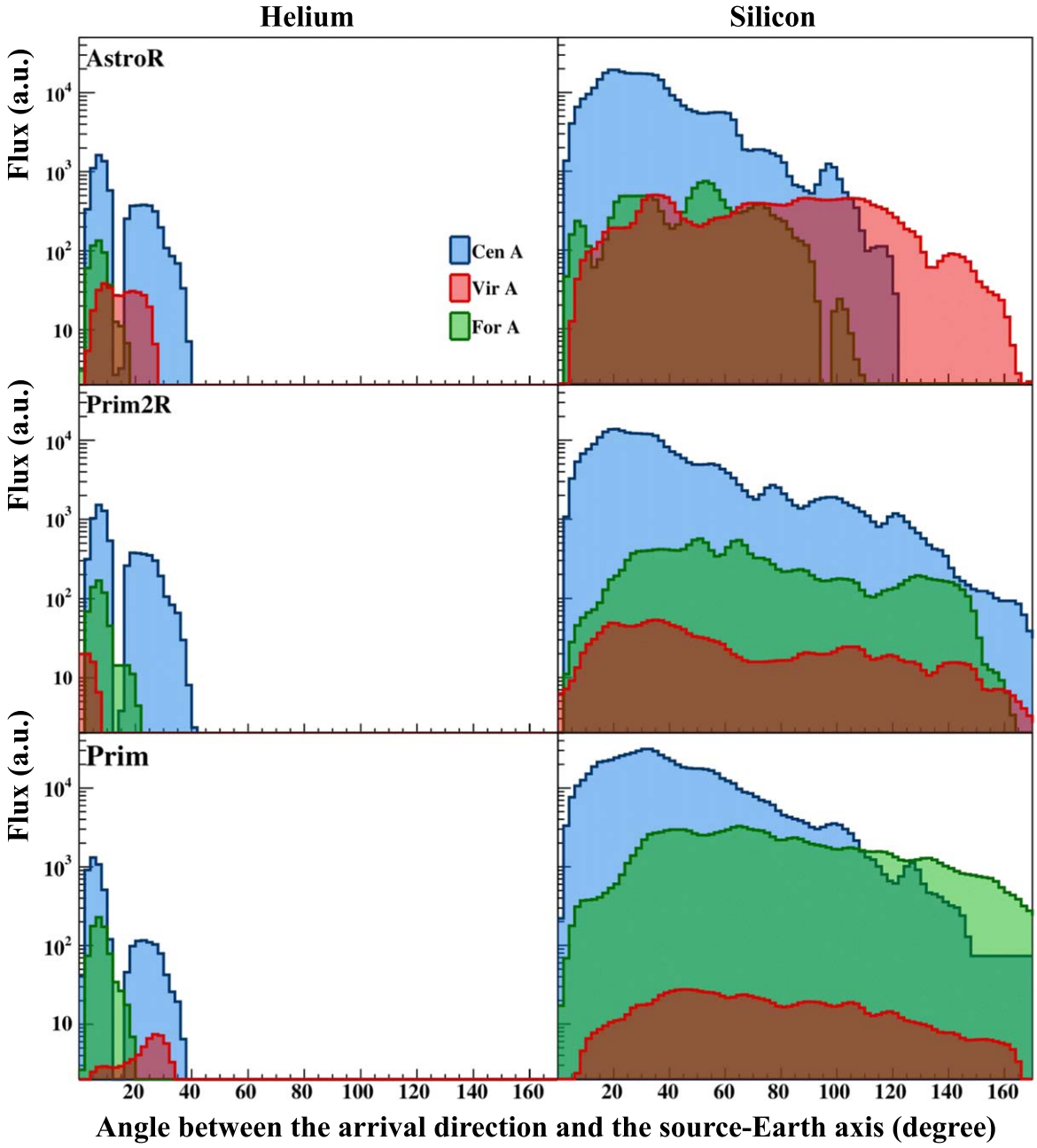

Figure 16. Angular distribution of events with $E > 32$ EeV in relation to the source direction. Each line in the figure shows one EGMF model: AstroR, Prim2R, and Prim. Each column in the figure shows a different nucleus leaving the source: helium and silicon nuclei. Note that in each column of the figure, all nucleus fragments on the way to Earth are shown as arriving at Earth although only helium and silicon nuclei left the source The three sources are shown by different colors: blue, red, and green for Cen A, Vir A, and For A. The sources are considered to output the same UHECR flux.

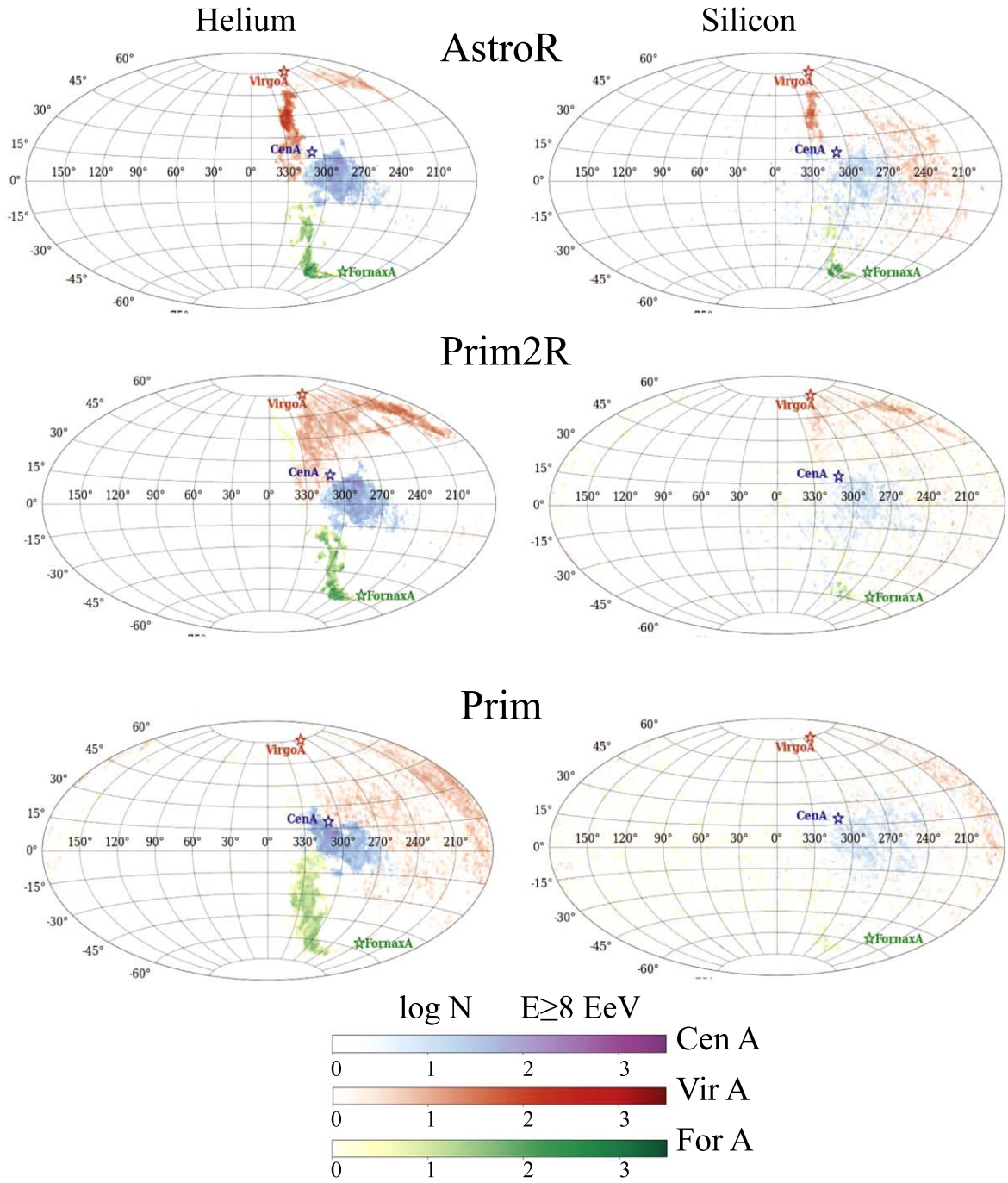

Figure 17. Sky maps in Galactic coordinates and Aitoff projections of all simulated events that arrived at Earth with energy above 8 EeV. Each line in the figure shows one of the EGMF models considered here. Each column in the figure shows a different nucleus leaving the source: helium and silicon nuclei. Note that in each column of the figure, all nucleus fragments on the way to Earth are shown as arriving at Earth when only helium or silicon nuclei left the source. The three sources are shown as blue, red, and green stars for Cen A, Vir A, and For A, respectively. The flux of events follows the same color coding, each color representing only the events generated in the respective source.

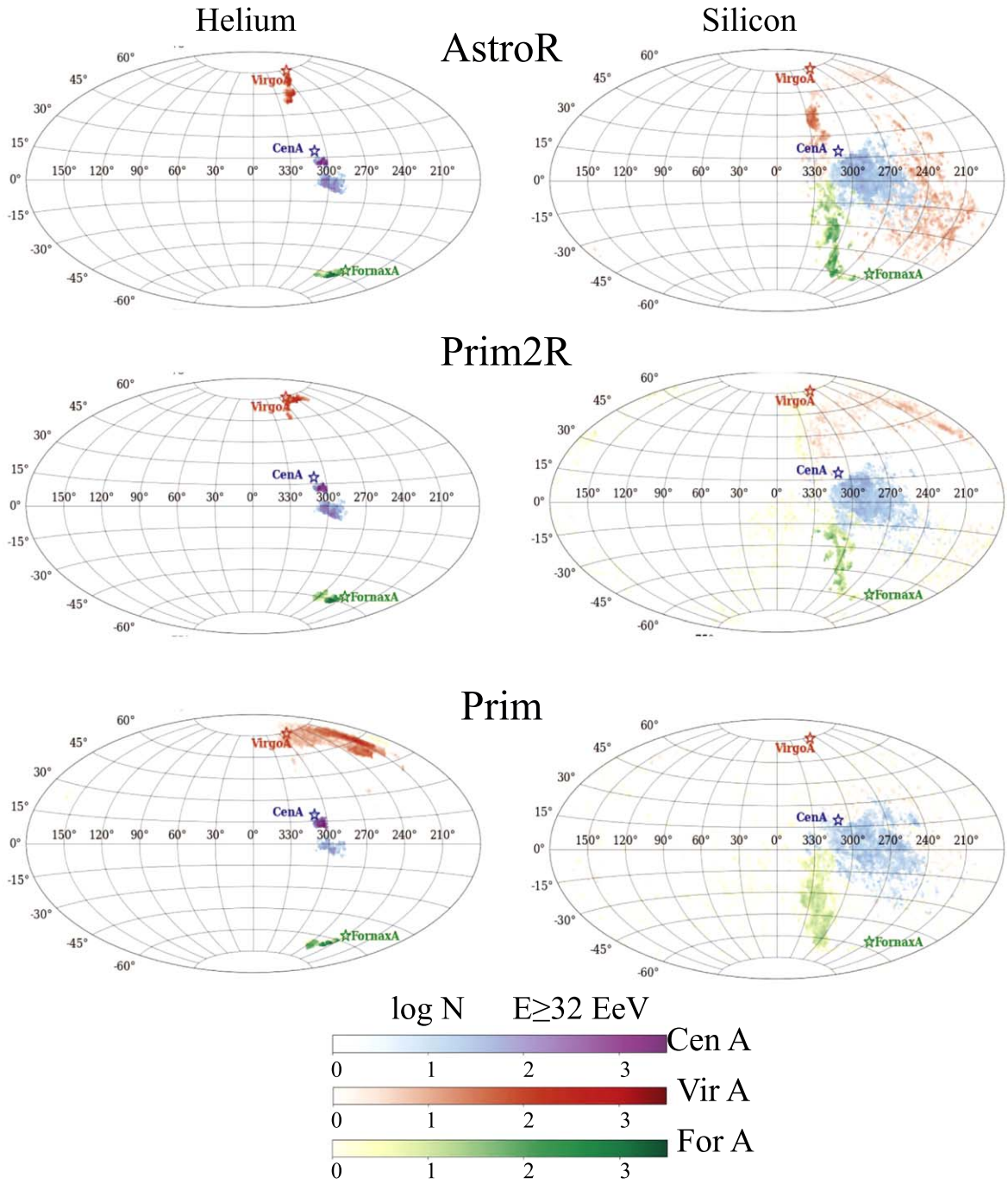

Figure 18. Sky maps in Galactic coordinates and Aitoff projections of all simulated events that arrived at Earth with energy above 32 EeV. Each line in the figure shows one of the EGMF models considered here. Each column in the figure shows a different nucleus leaving the source: helium and silicon nuclei. Note that in each column of the figure, all nucleus fragments on the way to Earth are shown as arriving at Earth when only helium or silicon nuclei left the source. The three sources are shown as blue, red, and green stars for Cen A, Vir A, and For A, respectively. The flux of events follows the same color coding, each color representing only the events generated in the respective source.

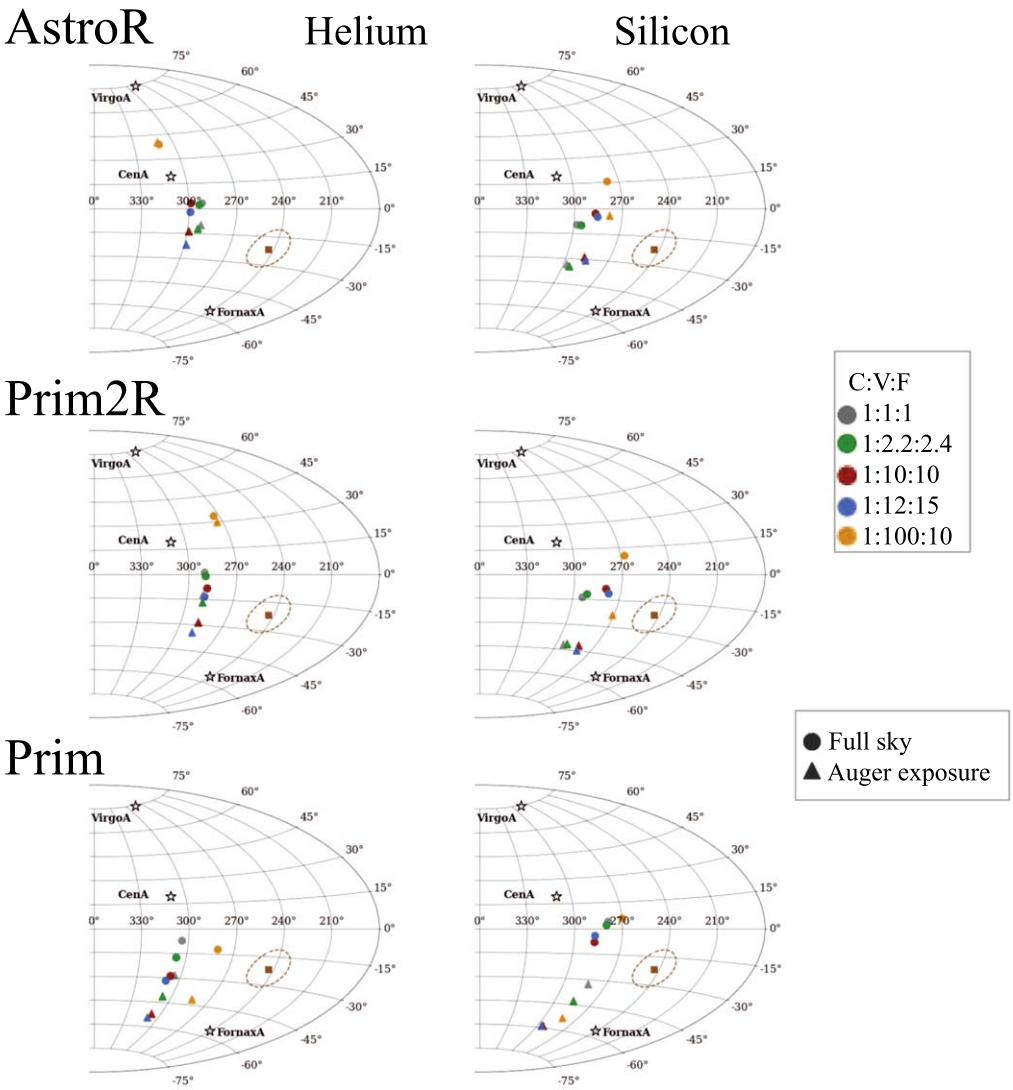

Figure 19. Sky maps in Galactic coordinates and Aitoff projections showing the dipole direction for the events with energy above 8 EeV. Each line in the figure shows one of the EGMF models considered here. Each column in the figure shows a different nucleus leaving the source: helium and silicon nuclei. Note that in each column of the figure, all nucleus fragments on the way to Earth are shown as arriving at Earth when only helium or silicon nuclei left the source. The three sources are shown as stars. The brown square shows the direction of the dipole measured by the Pierre Auger Observatory, and the dashed brown line shows its 1σ uncertainty. Colored circles show the direction of the dipoles calculated with the simulated events from Cen A, Vir A, and For A. Each color corresponds to a ratio of the flux emitted by Cen A:Vir A:For A as given in the legend.

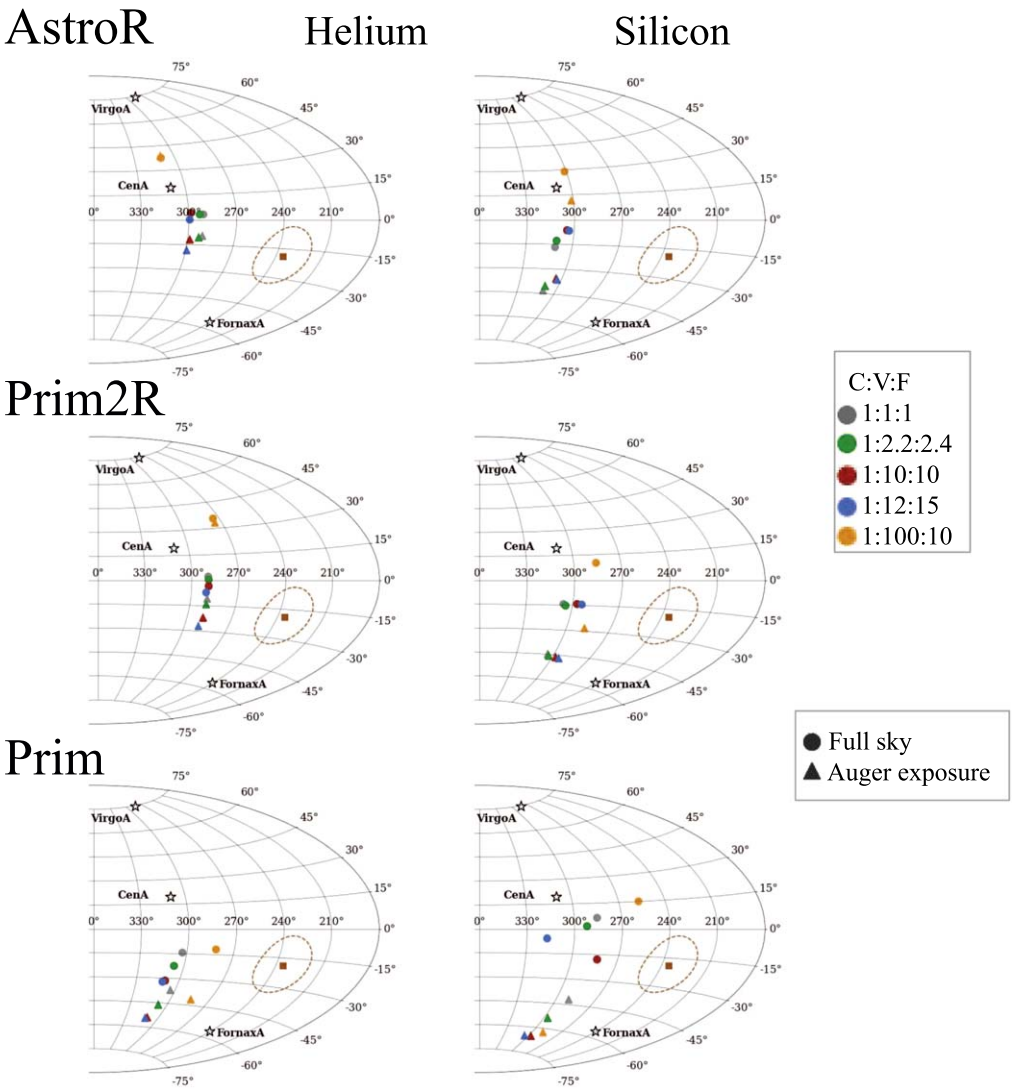

Figure 20. Sky maps in Galactic coordinates and Aitoff projections showing the dipole direction for the events with energy between 8 and 16 EeV. Each line in the figure shows one of the EGMF models considered here. Each column in the figure shows a different nucleus leaving the source: helium and silicon nuclei. Note that in each column of the figure, all nucleus fragments on the way to Earth are shown as arriving at Earth although only helium or silicon nuclei left the source. The three sources are shown as stars. The brown square shows the direction of the dipole measured by the Pierre Auger Observatory, and the dashed brown line shows its 1σ uncertainty. Colored circles show the direction of the dipoles calculated with the simulated events from Cen A, Vir A, and For A. Each color corresponds to a ratio of the flux emitted by Cen A:Vir A:For A as given in the legend.

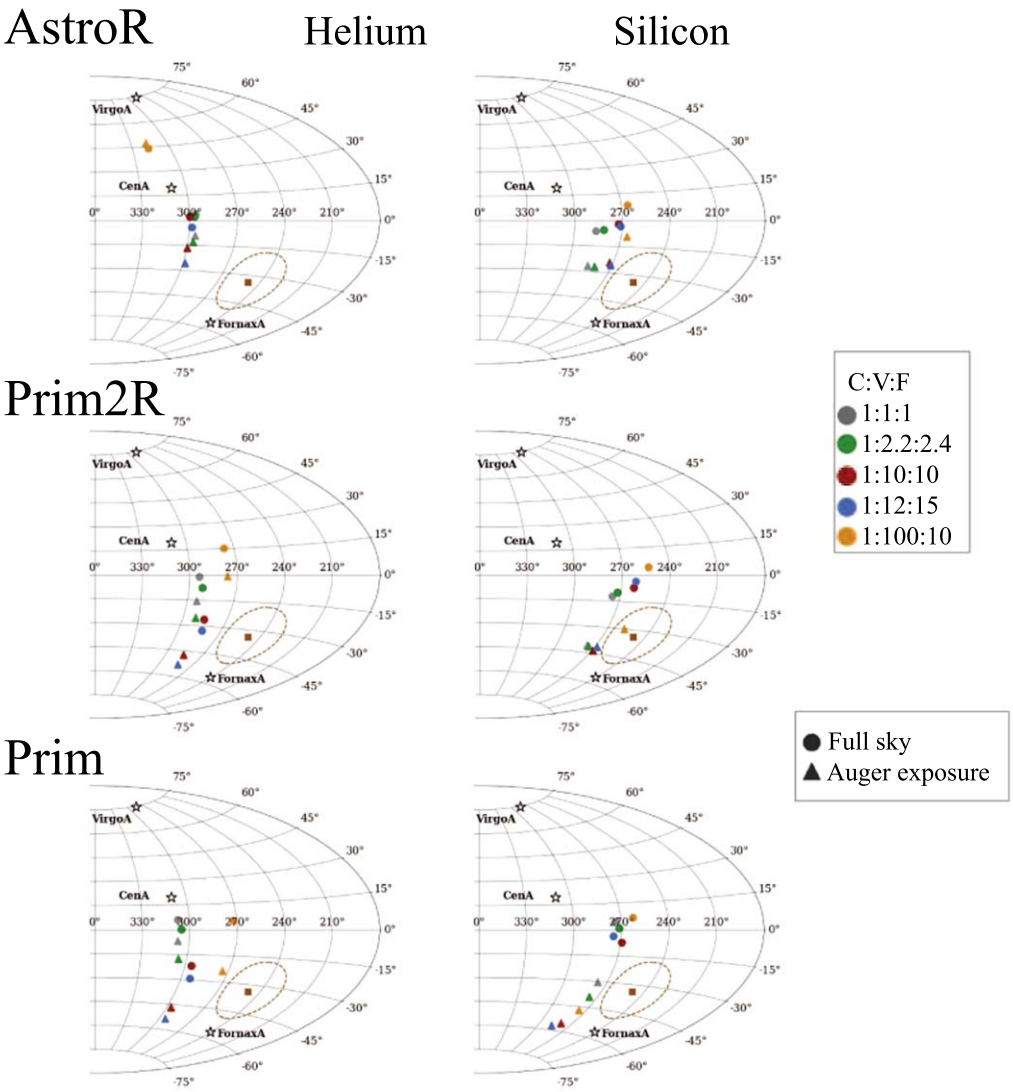

Figure 21. Sky maps in Galactic coordinates and Aitoff projections showing the dipole direction for the events with energy between 16 and 32 EeV. Each line in the figure shows one of the EGMF models considered here. Each column in the figure shows a different nucleus leaving the source: helium and silicon nuclei. Note that in each column of the figure, all nucleus fragments on the way to Earth are shown as arriving at Earth although only helium or silicon nuclei left the source. The three sources are shown as stars. The brown square shows the direction of the dipole measured by the Pierre Auger Observatory, and the dashed brown line shows its 1σ uncertainty. Colored circles show the direction of the dipoles calculated with the simulated events from Cen A, Vir A, and For A. Each color corresponds to a ratio of the flux emitted by Cen A:Vir A:For A as given in the legend.

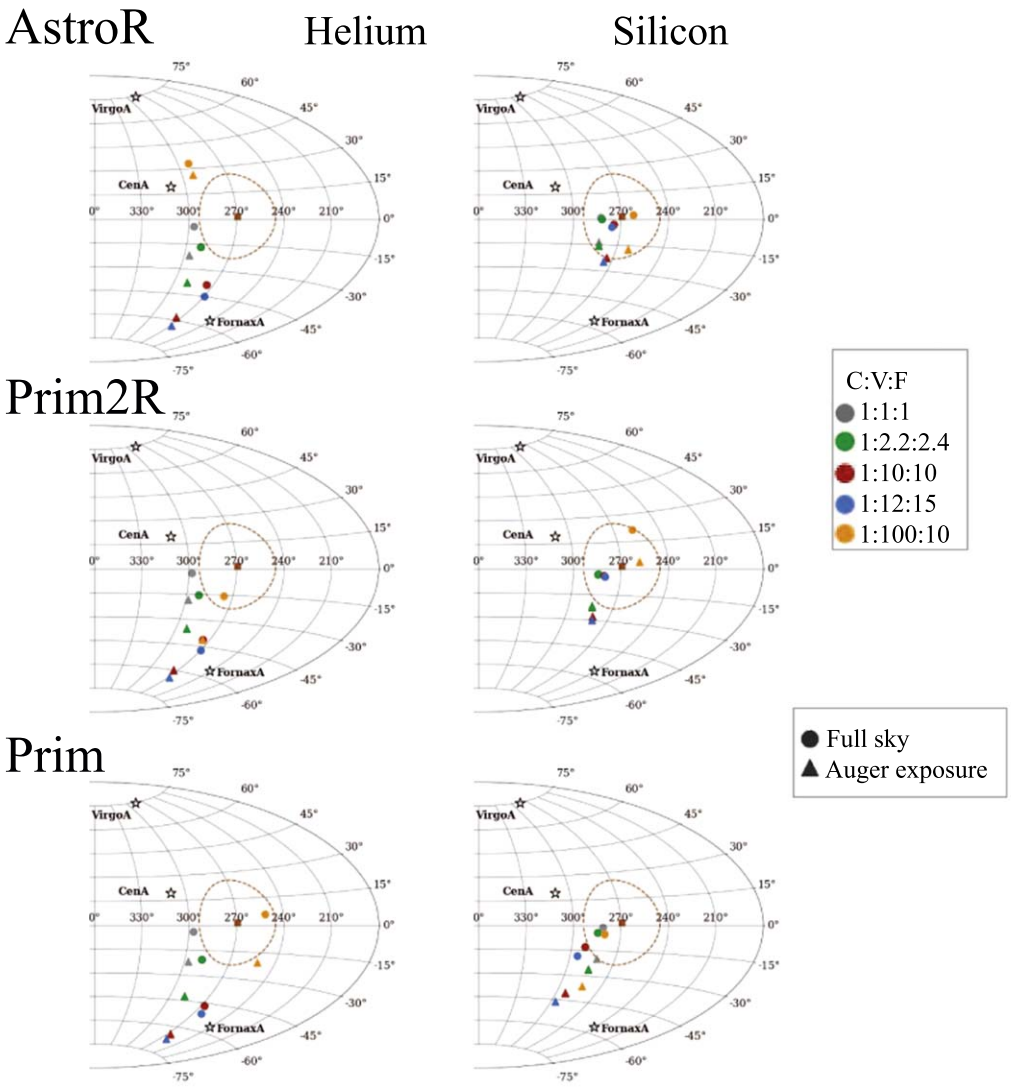

Figure 22. Sky maps in Galactic coordinates and Aitoff projections of all simulated events which arrived at Earth with energy above 32 EeV. Each line in the figure shows one of the EGMF models considered here. Each column in the figure shows a different nucleus leaving the source: helium and silicon nuclei. Note that in each column of the figure, all nucleus fragments on the way to Earth are shown as arriving at Earth when only helium or silicon nuclei left the source. The three sources are shown as stars. The brown square shows the direction of the dipole measured by the Pierre Auger Observatory, and the dashed brown line shows its 1σ uncertainty. Colored circles show the direction of the dipoles. Each color corresponds to a ratio of the flux emitted by Cen A:Vir A:For A as given in the legend.

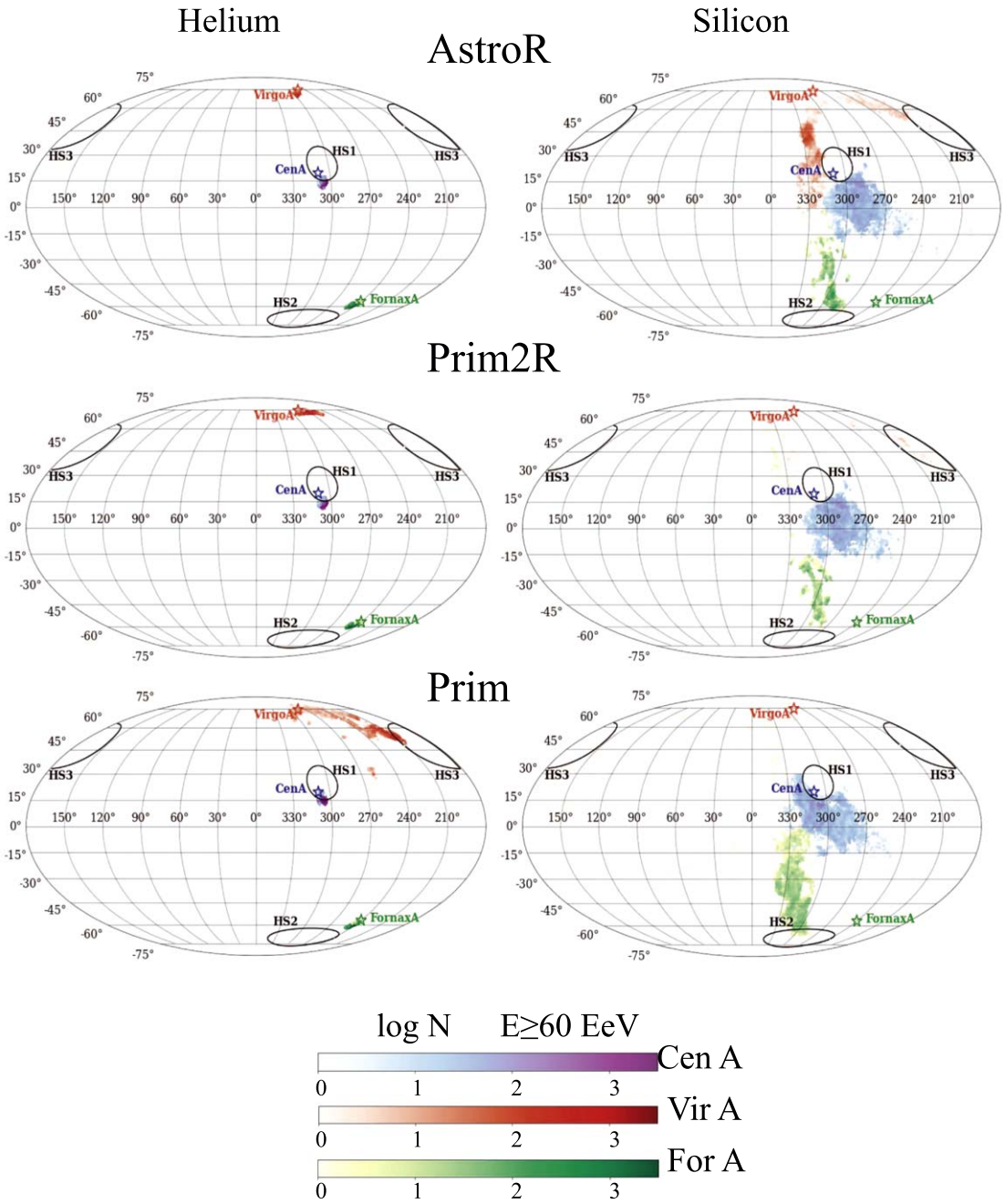

Figure 23. Sky maps in Galactic coordinates and Mollweide projections of all simulated events that arrived at Earth with energy above 60 EeV. Each line in the figure shows one of the EGMF models considered here. Each column in the figure shows a different nucleus leaving the source: helium and silicon nuclei. Note that in each column of the figure, all nucleus fragments on the way to Earth are shown as arriving at Earth when only helium or silicon nuclei left the source. The three sources are shown as blue, red, and green stars for Cen A, Vir A, and For A, respectively. The flux of events follows the same color coding, each color representing only the events generated in the respective source. The three hotspot regions are circulated by black full lines.

Appendix C
Dipole Direction

The dipole reconstruction was done from the simulated data set for each energy bin considered. From the possible approaches to reconstructing the dipole (Ding et al. 2021), the method of Aublin & Parizot (2005) was used for partial and full-sky exposure. For the case of partial exposure evaluation, the conditions established by the Pierre Auger Observatory (The Pierre Auger Collaboration 2018b) were reproduced, considering events with decl. δ between $-90° \leqslant \delta \leqslant 45°$. The results are summarized in Tables 1, 2, 3, and 4.

Table 1
Dipole Direction in Galactic Coordinates (l, b) in Degrees. $\geqslant$8 EeV—Partial Exposure/Full Sky

	H			He			N		
C:V:F	AstroR	Prim2R	Prim	AstroR	Prim2R	Prim	AstroR	Prim2R	Prim
1:1:1	(297,−8.8)	(294,−17)	(306,−8.2)	(292,−9.6)	(290,−12)	(305,−28)	(286,−21)	(281,−32)	(278,−29)
	(297,4.2)	(294,−2.0)	(306,5.8)	(292,3.1)	(290,1.2)	(304,−7.0)	(286,−3.1)	(280,−7.9)	(276,0.6)
1:2.2:2.4	(297,−14)	(291,−28)	(303,−20)	(294,−12)	(290,−16)	(307,−41)	(284,−22)	(280,−35)	(280,−34)
	(297,1.5)	(291,−9.7)	(302,−0.2)	(294,2.3)	(290,−1.2)	(307,−17)	(284,−2.4)	(278,−7.8)	(277,−0.7)
1:10:10	(299,−17)	(283,−51)	(290,−48)	(299,−13)	(288,−28)	(309,−52)	(277,−23)	(274,−39)	(287,−51)
	(299,2.7)	(283,−30)	(288,−21)	(299,3.3)	(288,−8.2)	(307,−29)	(277,−1.9)	(270,−6.8)	(281,−11)
1:12:15	(297,−28)	(281,−57)	(287,−55)	(299,−21)	(289,−34)	(311,−54)	(276,−24)	(275,−40)	(291,−53)
	(297,−5.6)	(281,−37)	(285,−28)	(299,−2.2)	(289,−13)	(310,−32)	(276,−2.8)	(270,−6.4)	(286,−12)
1:100:10	(316,51)	(275,−7.9)	(254,0.2)	(311,41)	(274,30)	(284,−41)	(270,−4.7)	(261,−16)	(277,−40)
	(316,47)	(275,22)	(252,22)	(311,39)	(274,34)	(281,−12)	(270,12)	(258,13)	(268,6.7)
	Si			**Fe**			**All**		
C:V:F	AstroR	Prim2R	Prim	AstroR	Prim2R	Prim	AstroR	Prim2R	Prim
1:1:1	(298,−33)	(295,−42)	(283,−32)	(302,−42)	(305,−49)	(284,−43)	(294,−26)	(294,−37)	(284,−30)
	(298,−9.7)	(294,−14)	(279,4.0)	(302,−12)	(306,−15)	(278,1.2)	(294,−4.8)	(293,−8.7)	(281,2.0)
1:2.2:2.4	(295,−34)	(292,−42)	(286,−43)	(298,−40)	(302,−50)	(291,−53)	(293,−25)	(290,−38)	(288,−43)
	(295,−9.9)	(291,−12)	(280,1.9)	(298,−9.4)	(302,−15)	(282,0.2)	(293,−3.2)	(289,−9.1)	(284,−4.3)
1:10:10	(288,−29)	(283,−42)	(295,−59)	(289,−37)	(293,−50)	(297,−65)	(287,−26)	(283,−41)	(296,−58)
	(287,−3.0)	(280,−8.5)	(287,−8.0)	(288,−3.8)	(290,−12)	(283,−24)	(287,−1.7)	(280,−10)	(290,−19)
1:12:15	(286,−30)	(282,−45)	(297,−59)	(290,−40)	(290,−51)	(301,−62)	(286,−28)	(282,−46)	(299,−60)
	(286,−4.7)	(278,−11)	(287,−4.0)	(288,−6.2)	(285,−14)	(294,−4.7)	(286,−3.4)	(279,−15)	(295,−22)
1:100:10	(278,−3.7)	(271,−23)	(284,−53)	(278,−15)	(281,−40)	(292,−61)	(282,6.4)	(271,−19)	(279,−50)
	(277,16)	(268,10)	(270,5.8)	(275,18)	(275,5.5)	(274,2.0)	(281,22)	(267,14)	(268,0.5)

Auger Experimental Data (The Pierre Auger Collaboration 2021): (243,−21)

Table 2
Dipole Direction in Galactic Coordinates (l, b) in Degrees. 8−16 EeV—Partial Exposure/Full Sky

	H			He			N		
C:V:F	AstroR	Prim2R	Prim	AstroR	Prim2R	Prim	AstroR	Prim2R	Prim
1:1:1	(297,−7.0)	(294,−12)	(308,−5.5)	(291,−9.3)	(290,−10.4)	(304,−37)	(287,−26)	(278,−39)	(277,−30)
	(297,5.0)	(294,0.9)	(308,7.0)	(291,3.3)	(290,2.4)	(303,−14)	(287,−5.6)	(277,−11)	(274,4.3)
1:2.2:2.4	(298,−9.4)	(293,−20)	(306,−14)	(293,−10)	(290,−14)	(308,−46)	(283,−24)	(276,−39)	(278,−40)
	(298,4.3)	(293,−3.7)	(305,3.1)	(293,3.4)	(290,0.5)	(307,−22)	(283,−3.1)	(273,−8.2)	(273,−0.8)
1:10:10	(303,−7.6)	(289,−38)	(296,−40)	(299,−12)	(289,−22)	(311,−54)	(275,−21)	(271,−38)	(285,−55)
	(303,8.1)	(289,−18)	(295,−13)	(299,4.1)	(289,−3.4)	(310,−31)	(275,0.2)	(264,−0.7)	(276,−7.6)
1:12:15	(302,−17)	(288,−45)	(294,−47)	(300,−18)	(291,−27)	(312,−54)	(275,−22)	(271,−39)	(285,−55)
	(302,1.8)	(288,−24)	(292,−20)	(300,0.1)	(291,−6.9)	(312,−32)	(275,−0.7)	(263,−1.6)	(274,−9.3)
1:100:10	(318,50)	(274,24)	(263,−4.8)	(310,39)	(275,34)	(285,−41)	(270,−4.8)	(261,−25)	(274,−45)
	(318,45)	(274,31)	(260,18)	(310,38)	(275,36)	(282,−12)	(270,12)	(256,9.2)	(261,7.2)
	Si			**Fe**			**All**		
C:V:F	AstroR	Prim2R	Prim	AstroR	Prim2R	Prim	AstroR	Prim2R	Prim
1:1:1	(311,−43)	(305,−44)	(291,−42)	(309,−51)	(312,−56)	(301,−64)	(297,−29)	(297,−37)	(290,−36)
	(311,−17)	(306,−14)	(286,6.7)	(311,−12)	(317,−20)	(296,−18)	(297,−5.2)	(297,−8.2)	(287,0.9)
1:2.2:2.4	(310,−40)	(304,−45)	(297,−54)	(306,−50)	(312,−56)	(302,−64)	(296,−26)	(296,−40)	(292,−47)
	(311,−13)	(305,−15)	(292,1.9)	(308,−9.9)	(317,−19)	(297,−4.8)	(295,−2.1)	(295,−9.7)	(288,−4.3)
1:10:10	(305,−35)	(288,−46)	(298,−65)	(301,−46)	(303,−59)	(302,−68)	(294,−24)	(287,−42)	(300,−59)
	(305,−6.1)	(297,−14)	(284,−18)	(301,3.8)	(303,−24)	(294,−47)	(293,0.9)	(284,−8.9)	(297,−17)
1:12:15	(303,−36)	(295,−46)	(306,−65)	(300,−48)	(298,−61)	(302,−69)	(292,−27)	(284,−42)	(301,−63)
	(304,−6.4)	(294,−14)	(317,−5.7)	(300,−8.3)	(297,−28)	(292,−55)	(292,−1.5)	(280,−8.6)	(296,−28)
1:100:10	(301,12)	(288,−28)	(289,−62)	(299,−8.9)	(292,−52)	(292,−68)	(290,14)	(274,−13)	(281,−53)
	(301,29)	(286,11)	(257,15)	(298,39)	(286,5.4)	(223,22)	(289,28)	(271,20)	(266,−0.3)

Auger Experimental Data (The Pierre Auger Collaboration 2021): (235,−19)

Table 3
Dipole Direction in Galactic Coordinates (l, b) in Degrees. 16–32 EeV—Partial Exposure/Full Sky

	H			He			N		
C:V:F	AstroR	Prim2R	Prim	AstroR	Prim2R	Prim	AstroR	Prim2R	Prim
1:1:1	(297,−16)	(291,−45)	(289,−42)	(296,−8.9)	(294,−15)	(308,−6.7)	(280,−17)	(281,−30)	(279,−20)
	(297,1.4)	(291,−24)	(288,−15)	(296,3.7)	(294,−1.1)	(307,5.9)	(280,−1.2)	(281,−8.9)	(279,−1.2)
1:2.2:2.4	(292,−27)	(283,−58)	(278,−57)	(297,−13)	(292,−25)	(306,−17)	(278,−20)	(280,−33)	(280,−23)
	(292,−4.6)	(283,−39)	(277,−31)	(297,2.0)	(292,−7.6)	(305,0.1)	(278,−2.5)	(280,−11)	(279,−1.8)
1:10:10	(287,−36)	(271,−67)	(264,−66)	(300,−16)	(285,−47)	(297,−46)	(273,−27)	(276,−42)	(287,−39)
	(287,−9.0)	(271,−52)	(261,−44)	(300,2.0)	(285,−26)	(296,−22)	(273,−6.2)	(275,−16)	(284,−9.4)
1:12:15	(284,−45)	(270,−68)	(264,−68)	(299,−26)	(283,−53)	(295,−53)	(272,−32)	(275,−47)	(289,−44)
	(284,−19)	(270,−53)	(261,−48)	(299,−4.3)	(283,−33)	(294,−29)	(272,−10)	(273,−21)	(286,−13)
1:100:10	(307,60)	(274,−40)	(231,16.5)	(317,48)	(276,−0.5)	(274,−23)	(261,−11)	(255,−1.7)	(273,−28)
	(307,55)	(274,−14)	(230,30)	(317,44)	(276,15)	(272,5.0)	(261,6.9)	(254,19)	(268,4.8)
	Si			**Fe**			**All**		
C:V:F	AstroR	Prim2R	Prim	AstroR	Prim2R	Prim	AstroR	Prim2R	Prim
1:1:1	(286,−27)	(277,−41)	(277,−30)	(311,−45)	(303,−44)	(291,−38)	(292,−27)	(289,−37)	(283,−27)
	(286,−6.2)	(275,−12)	(274,4.2)	(311,−20)	(304,−13)	(286,11)	(292,−6.7)	(289,−11)	(281,2.2)
1:2.2:2.4	(282,−27)	(275,−41)	(276,−39)	(309,−43)	(301,−44)	(295,−51)	(288,−27)	(285,−40)	(285,−37)
	(282,−5.8)	(272,−10)	(272,0.8)	(309,−17)	(301,−12)	(289,11)	(288,−5.8)	(284,−12)	(281,−0.3)
1:10:10	(272,−24)	(270,−43)	(281,−55)	(304,−37)	(294,−40)	(300,−65)	(282,−28)	(277,−46)	(292,−54)
	(272,−2.2)	(263,−7.2)	(269,−7.3)	(304,−7.3)	(293,−5.6)	(286,3.0)	(282,−4.6)	(273,−15)	(286,−9.3)
1:12:15	(271,−26)	(269,−41)	(287,−57)	(303,−38)	(290,−40)	(304,−66)	(280,−32)	(275,−47)	(293,−58)
	(271,−3.5)	(261,−3.7)	(275,−3.7)	(303,−8.3)	(288,−4.1)	(312,−7.7)	(280,−7.7)	(271,−17)	(286,−14)
1:100:10	(267,−9.1)	(259,−30)	(277,−47)	(293,−8.2)	(288,−36)	(297,−63)	(274,1.9)	(265,−18)	(278,−46)
	(266,8.4)	(254,4.1)	(262,6.5)	(293,19)	(285,3.0)	(277,21)	(274,17)	(262,12)	(264,11)
Auger Experimental Data (The Pierre Auger Collaboration 2021): (248,−34)									

Table 4
Dipole Direction in Galactic Coordinates (l, b) in Degrees. $\geqslant$32 EeV—Partial Exposure/Full Sky

	H			He			N		
C:V:F	AstroR	Prim2R	Prim	AstroR	Prim2R	Prim	AstroR	Prim2R	Prim
1:1:1	(265,−63)	(264,−64)	(257,−61)	(297,−22)	(298,−18)	(297,−22)	(293,−7.6)	(292,−9.2)	(307,−23)
	(265,−45)	(264,−46)	(257,−42)	(297,−4.4)	(298,−2.6)	(297,−4.0)	(293,4.1)	(292,2.8)	(307,−5.6)
1:2.2:2.4	(259,−66)	(258,−66)	(250,−64)	(291,−38)	(292,−36)	(289,−42)	(294,−7.7)	(292,−11)	(309,−37)
	(259,−49)	(258,−51)	(250,−47)	(291,−17)	(292,−15)	(289,−20)	(294,4.3)	(292,1.6)	(309,−16)
1:10:10	(257,−66)	(254,−68)	(245,−65)	(275,−58)	(275,−60)	(268,−64)	(298,−8.4)	(292,−19)	(314,−52)
	(257,−50)	(254,−53)	(245,−48)	(275,−38)	(275,−41)	(267,−47)	(298,5.2)	(292,−2.9)	(313,−32)
1:12:15	(255,−68)	(253,−68)	(245,−67)	(270,−63)	(270,−64)	(263,−67)	(299,−14)	(292,−24)	(315,−54)
	(255,−52)	(253,−54)	(245,−51)	(270,−45)	(270,−47)	(263,−51)	(299,2.1)	(292,−6.4)	(315,−34)
1:100:10	(281,41)	(263,4.1)	(233,40)	(293,27)	(276,−41)	(252,−20)	(313,34)	(281,20)	(304,−48)
	(281,44)	(263,24)	(233,42)	(293,33)	(276,−16)	(252,5.9)	(313,34)	(281,26)	(303,−25)
	Si			**Fe**			**All**		
C:V:F	AstroR	Prim2R	Prim	AstroR	Prim2R	Prim	AstroR	Prim2R	Prim
1:1:1	(283,−13)	(285,−21)	(282,−20)	(284,−19)	(281,−32)	(277,−29)	(285,−14)	(285,−24)	(282,−24)
	(283,0.8)	(285,−3.5)	(282,−1.4)	(284,−2.2)	(280,−8.4)	(257,−0.4)	(285,0.6)	(285,−4.6)	(281,−0.6)
1:2.2:2.4	(282,−16)	(285,−22)	(285,−26)	(279,−20)	(279,−35)	(280,−34)	(283,−17)	(284,−25)	(284,−32)
	(282,−0.1)	(284,−3.2)	(285,−4.5)	(279,−2.1)	(278,−8.6)	(277,−0.8)	(283,−0.3)	(283,−4.3)	(283,−4.6)
1:10:10	(274,−22)	(282,−28)	(293,−41)	(270,−21)	(273,−35)	(284,−48)	(276,−22)	(278,−33)	(294,−47)
	(274,−3.3)	(281,−4.1)	(292,−13)	(270,−1.4)	(269,−2.6)	(277,−5.2)	(276,−2.6)	(276,−5.4)	(292,−15)
1:12:15	(276,−24)	(281,−30)	(297,−46)	(269,−22)	(273,−37)	(291,−53)	(275,−25)	(277,−36)	(295,−51)
	(276,−4.8)	(280,−4.8)	(295,−18)	(269,−2.1)	(267,−1.9)	(285,−9.9)	(275,−4.5)	(274,−7.6)	(293,−19)
1:100:10	(262,−17)	(258,4.0)	(284,−36)	(260,−18)	(260,−21)	(281,−45)	(265,−11)	(261,−6.7)	(285,−40)
	(262,2.2)	(258,21)	(280,−5.3)	(260,1.2)	(257,9.6)	(273,−0.4)	(265,6.3)	(259,16)	(281,−4.2)
Auger Experimental Data (The Pierre Auger Collaboration 2021): (269,1.4)									

ORCID iDs

Cainã de Oliveira https://orcid.org/0000-0003-4038-1509
Vitor de Souza https://orcid.org/0000-0003-0865-233X

References

Aloisio, R., & Berezinsky, V. 2004, ApJ, 612, 900
Aublin, J., & Parizot, E. 2005, A&A, 441, 407
Batista, R. A., & Sigl, G. 2014, JCAP, 2014, 031
Batista, R. A., Dundovic, A., Erdmann, M., et al. 2016, JCAP, 2016, 038
Bell, A., Araudo, A., Matthews, J., & Blundell, K. 2018, MNRAS, 473, 2364
Biermann, P. L., & De Souza, V. 2012, ApJ, 746, 72
Biermann, P. L., De Souza, V., Wiita, P. J., et al. 2010, ApJL, 720, L155
Bretz, H.-P., Erdmann, M., Schiffer, P., Walz, D., & Winchen, T. 2014, APh, 54, 110
Burns, J. O., Feigelson, E., & Schreier, E. 1983, ApJ, 273, 128
Cavagnolo, K. W., McNamara, B. R., Nulsen, P. E. J., et al. 2010, ApJ, 720, 1066
Cho, J., & Ryu, D. 2009, ApJL, 705, L90
Das, S., Kang, H., Ryu, D., & Cho, J. 2008, ApJ, 682, 29
de Oliveira, C., & de Souza, V. 2021, EPJC, 81, 1
Dermer, C. D., & Razzaque, S. 2010, ApJ, 724, 1366
Ding, C., Globus, N., & Farrar, G. R. 2021, ApJL, 913, L13
Dolag, K., Kachelrieß, M., & Semikoz, D. 2009, JCAP, 2009, 033
Durrer, R., & Neronov, A. 2013, A&ARv, 21, 62
Eckert, D., et al. 2015, Natur, 528, 105
Eichmann, B. 2019, JCAP, 2019, 009
Eichmann, B., Rachen, J., Merten, L., van Vliet, A., & Tjus, J. B. 2018, JCAP, 2018, 036
Erdmann, M., Müller, G., Urban, M., & Wirtz, M. 2016, APh, 85, 54
Farrar, G. R., Jansson, R., Feain, I. J., & Gaensler, B. 2013, JCAP, 2013, 023
Feigelson, E., Schreier, E., Delvaille, J., et al. 1981, ApJ, 251, 31
Ferrarese, L., Cote, P., Jordan, A., et al. 2006, ApJS, 164, 334
Ghisellini, G., Ghirlanda, G., Tavecchio, F., Fraternali, F., & Pareschi, G. 2008, MNRAS, 390, L88
Gilmore, R. C., Somerville, R. S., Primack, J. R., & Domínguez, A. 2012, MNRAS, 422, 3189
Ginzburg, V., & Syrovatskii, S. 1963, SvA, 7, 357
Godfrey, L., & Shabala, S. 2016, MNRAS, 456, 1172
Godfrey, L. E. H., & Shabala, S. S. 2015, MNRAS, 456, 1172
Greisen, K. 1966, PhRvL, 16, 748
Hackstein, S., Vazza, F., Brüggen, M., Sigl, G., & Dundovic, A. 2016, MNRAS, 462, 3660
Hackstein, S., Vazza, F., Brüggen, M., Sorce, J. G., & Gottlöber, S. 2018, MNRAS, 475, 2519
Hada, K. 2013, EPJWC, 61, 01002
Halzen, F., & Hooper, D. 2002, RPPh, 65, 1025
Hardcastle, M., Worrall, D., Kraft, R., et al. 2003, ApJ, 593, 169
Hillas, A. M. 1984, ARA&A, 22, 425
Israel, F. 1998, A&ARv, 8, 237
Jansson, R., & Farrar, G. R. 2012, ApJ, 757, 14
Jensen, J. B., Tonry, J. L., Barris, B. J., et al. 2003, ApJ, 583, 712
Kachelriess, M., Ostapchenko, S., & Tomas, R. 2009, NJPh, 11, 065017
Kino, M., Takahara, F., Hada, K., & Doi, A. 2013, EPJWC, 61, 01009
Kobzar, O., Hnatyk, B., Marchenko, V., & Sushchov, O. 2019, MNRAS, 484, 1790
Kotera, K., & Olinto, A. V. 2011, ARA&A, 49, 119
Kraft, R. P., Forman, W. R., Jones, C., et al. 2002, ApJ, 569, 54
Kronberg, P. P. 1994, RPPh, 57, 325
Lang, R. G., Taylor, A. M., Ahlers, M., & de Souza, V. 2020, PhRvD, 102, 063012
Lang, R. G., Taylor, A. M., & de Souza, V. 2021, PhRvD, 103 063005
Lee, S., Olinto, A. V., & Sigl, G. 1995, ApJL, 455, L21
Maccagni, F. M., Murgia, M., Serra, P., et al. 2020, A&A, 634, A9
Macchetto, F., Marconi, A., Axon, D. J., et al. 1997, ApJ, 489, 579
Mannheim, K., & Biermann, P. L. 1989, A&A, 221, 211
Matthews, J. H., Bell, A. R., Blundell, K. M., & Araudo, A. T. 2018, MNRAS, 479, L76
Matthews, J. H., Bell, A. R., Blundell, K. M., & Araudo, A. T. 2019, MNRAS, 482, 4303
Norman, C. A., Melrose, D. B., & Achterberg, A. 1995, ApJ, 454, 60
Nowak, N., Saglia, R. P., Thomas, J., et al. 2008, MNRAS, 391, 1629
Olinto, A. 2000, PhR, 333, 329
Pacholczyk, A. G. 1970, Radio Astrophysics: Nonthermal Processes in Galactic and Extragalactic Sources (San Francisco, CA: W.H. Freeman & Co Ltd.)
Rachen, J. P. 2008, arXiv:0808.0349
Rachen, J. P., & Biermann, P. L. 1993, A&A, 272, 161
Rachen, J. P., & Mészáros, P. 1998, PhRvD, 58, 123005
Rejkuba, M. 2004, A&A, 413, 903
Romero, G. E., Combi, J. A., Perez Bergliaffa, S. E., & Anchordoqui, L. A. 1996, APh, 5, 279
Röser, H.-J., & Meisenheimer, K. (ed.) 1997, The Radio Galaxy Messier 87 (Berlin: Springer)
Ryu, D., Kang, H., Cho, J., & Das, S. 2008, Sci, 320, 909
Schweizer, F. 1980, ApJ, 237, 303
Sigl, G., Miniati, F., & Ensslin, T. A. 2003, PhRvD, 68, 043002
Sigl, G., Miniati, F., & Ensslin, T. A. 2004, NuPhS, 136, 224
Snios, B., Nulsen, P. E. J., Kraft, R. P., et al. 2019, ApJ, 879, 8
Subramanian, K. 2016, RPPh, 79, 076901
Sun, Xiao-na, Yang, Rui-zhi, Mckinley, Benjamin, & Aharonian, Felix 2016, A&A, 595, A29
Supanitsky, A. D., & de Souza, V. 2013, JCAP, 2013, 023
Tanco, G. A. M. 1998, ApJL, 505, L79
Tanco, G. M. 2001, in Cosmic Magnetic Fields from the Perspective of Ultra-High-Energy Cosmic Rays Propagation, ed. M. Lemoine & G. Sigl, Vol. 155 (Berlin: Springer)
Taylor, A. M., Ahlers, M., & Aharonian, F. A. 2011, PhRvD, 84 105007
The H.E.S.S. Collaboration, et al. 2020, Natur, 582, 356
The Pierre Auger and Telescope Array Collaborations 2019, ICRC (Madison, WI), 358, 234
The Pierre Auger Collaboration 2015, NIMPA, 798, 172
The Pierre Auger Collaboration 2017, Sci, 357, 1266
The Pierre Auger Collaboration 2018a, ApJL, 853, L29
The Pierre Auger Collaboration 2018b, ApJ, 868, 4
The Pierre Auger Collaboration 2021, ICRC (Berlin), 395, 335
The Pierre Auger Observatory 2020, JInst, 15, P10021
The Telescope Array Collaboration 2008, NuPhS, 175, 221
The Telescope Array Collaboration 2014, ApJL, 790, L21
The Telescope Array Collaboration 2020, ApJ, 899, 86
van Velzen, S., Falcke, H., Schellart, P., Nierstenhöfer, N., & Kampert, K.-H. 2012, A&A, 544, A18
Vietri, M. 1995, ApJ, 453, 883
Wang, X.-Y., Razzaque, S., & Mészáros, P. 2008, ApJ, 677, 432
Waxman, E. 1995, PhRvL, 75, 386
Waxman, E., & Miralda-Escudé, J. 1996, ApJL, 472, L89
Widrow, L. M., Ryu, D., Schleicher, D. R., et al. 2012, SSRv, 166, 37
Willott, C. J., Rawlings, S., Blundell, K. M., & Lacy, M. 1999, MNRAS, 309, 1017
Wykes, S., Croston, J. H., Hardcastle, M. J., et al. 2013, A&A, 558, A19
Yang, R.-Z., Sahakyan, N., de Ona Wilhelmi, E., Aharonian, F., & Rieger, F. 2012, A&A, 542, A19
Zatsepin, G. T., & Kuz'min, V. A. 1966, JETPL, 4, 78